

A human-specific modifier of cortical connectivity and circuit function

<https://doi.org/10.1038/s41586-021-04039-4>

Received: 22 November 2019

Accepted: 17 September 2021

Published online: 27 October 2021

 Check for updates

Ewoud R. E. Schmidt^{1,2,6}, Hanzhi T. Zhao^{2,3,6}, Jung M. Park^{1,2}, Mario Dipoppa^{2,4,7}, Mauro M. Monsalve-Mercado^{2,4,7}, Jacob B. Dahan^{1,2}, Chris C. Rodgers^{1,2,5}, Amélie Lejeune^{1,2}, Elizabeth M. C. Hillman^{2,3}, Kenneth D. Miller^{1,2,4,5}, Randy M. Bruno^{1,2,5} & Franck Polleux^{1,2,5}✉

The cognitive abilities that characterize humans are thought to emerge from unique features of the cortical circuit architecture of the human brain, which include increased cortico–cortical connectivity. However, the evolutionary origin of these changes in connectivity and how they affected cortical circuit function and behaviour are currently unknown. The human-specific gene duplication *SRGAP2C* emerged in the ancestral genome of the *Homo* lineage before the major phase of increase in brain size^{1,2}. *SRGAP2C* expression in mice increases the density of excitatory and inhibitory synapses received by layer 2/3 pyramidal neurons (PNs)^{3–5}. Here we show that the increased number of excitatory synapses received by layer 2/3 PNs induced by *SRGAP2C* expression originates from a specific increase in local and long-range cortico–cortical connections. Mice humanized for *SRGAP2C* expression in all cortical PNs displayed a shift in the fraction of layer 2/3 PNs activated by sensory stimulation and an enhanced ability to learn a cortex-dependent sensory-discrimination task. Computational modelling revealed that the increased layer 4 to layer 2/3 connectivity induced by *SRGAP2C* expression explains some of the key changes in sensory coding properties. These results suggest that the emergence of *SRGAP2C* at the birth of the *Homo* lineage contributed to the evolution of specific structural and functional features of cortical circuits in the human cortex.

In recent years, a growing number of human-specific genetic modifiers have been identified—such as human-specific gene duplications^{6,7}—that can induce human-specific traits of brain development. The first experimental test of this idea came from studies of the human-specific gene duplication affecting the ancestral gene Slit-Robo GTPase activating protein 2A (*SRGAP2A*). Duplication of *SRGAP2A* specifically in the human lineage led to the emergence of the human-specific paralogue *SRGAP2C*^{3,4}. When expressed in mouse cortical PNs in vivo, *SRGAP2C* inhibits the functions of ancestral *SRGAP2A*, a postsynaptic protein that regulates excitatory and inhibitory synapse maturation and density in cortical PNs. Because of the truncation of the last 49 amino acids of its F-BAR domain, *SRGAP2C* is intrinsically unstable but is still able to dimerize with the F-BAR domain of *SRGAP2A* and thereby reduce *SRGAP2A* levels through proteasome-dependent degradation^{5,8}. The expression of human-specific *SRGAP2C* in mouse layer 2/3 PNs induces changes in synaptic development that phenocopy a partial loss of function of *SRGAP2A* and mimic synaptic features characterizing human cortical PNs. These include similar increases in the density of both excitatory and inhibitory synapses received by layer 2/3 PNs and neonatal features of excitatory and inhibitory synaptic development^{3–5}. These findings indicate that mouse cortical PNs expressing *SRGAP2C* receive an increased number of synaptic inputs, similar to what is observed in human PNs^{9,10}. *SRGAP2C* may therefore act as a human-specific modifier of cortical connectivity in the human brain.

Here, we use a new humanized mouse model expressing *SRGAP2C* in all cortical glutamatergic neurons (*SRGAP2C* mice) together with quantitative monosynaptic rabies virus (RABV) tracing, in vivo two-photon Ca²⁺ imaging, computational modelling approaches and a new behavioural paradigm to investigate how humanization of *SRGAP2C* expression modifies cortical circuit connectivity and function and behavioural performance.

Mapping of connectivity in *SRGAP2C* mice

We developed a new transgenic mouse line (*Rosa26-loxP-STOP-loxP-SRGAP2C-HA* knock-in) that enables the spatial and temporal control of *SRGAP2C* expression in a Cre-dependent manner (Extended Data Fig. 1). To determine the origin of increased connectivity received by layer 2/3 PNs following *SRGAP2C* expression, we devised a strategy that uses sparse in utero cortical electroporation (IUCE) combined with monosynaptic RABV tracing^{11,12} (Fig. 1a, b). IUCE experiments were performed with a low amount of plasmid encoding Cre recombinase (Methods), which led to the sparse expression of *SRGAP2C* in a small number of layer 2/3 cortical PNs in the primary somatosensory cortex (barrel cortex; S1) that were primed for RABV infection (termed ‘starter’ neurons). Adult mice (aged more than postnatal day 65 (P65)) were stereotactically injected with RABV (Fig. 1a). Whole mouse brains were

¹Department of Neuroscience, Columbia University, New York, NY, USA. ²Mortimer B. Zuckerman Mind Brain Behavior Institute, Columbia University, New York, NY, USA. ³Department of Biomedical Engineering and Radiology, Columbia University, New York, NY, USA. ⁴Center for Theoretical Neuroscience, College of Physicians and Surgeons, Columbia University, New York, NY, USA. ⁵Kavli Institute for Brain Science, Columbia University, New York, NY, USA. ⁶Present address: Department of Neuroscience, Medical University of South Carolina, Charleston, SC, USA.

⁷These authors contributed equally: Mario Dipoppa, Mauro M. Monsalve-Mercado. ✉e-mail: fp2304@columbia.edu

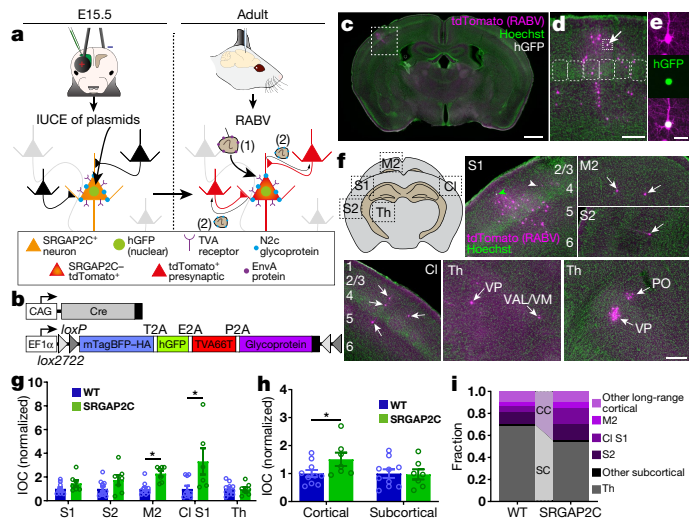


Fig. 1 | Sparse monosynaptic tracing in layer 2/3 PNs humanized for SRGAP2C expression. **a**, Left, the BHTG construct (schematic in **b**), together with Cre recombinase, is targeted to layer 2/3 cortical PNs in S1 by IUCE at embryonic day 15.5 (E15.5). Right, stereotaxic injection of RABV (CVS-N2c^{ΔG}) in adult mice leads to infection of starter neurons (1), after which it spreads to presynaptically connected neurons (2). **b**, Schematics of the BHTG and Cre constructs. **c**, Coronal section stained for Hoechst (green) showing the location of a starter neuron (dashed white box) in the barrel field of the primary sensory cortex (S1). Scale bar, 1 mm. **d**, Higher magnification of the dashed white box area in **c**. A starter neuron is indicated by the white arrow. Rounded boxes indicate barrels in layer 4. Scale bar, 200 μ m. **e**, High magnification images of a starter neuron. Scale bar, 25 μ m. **f**, Schematic (top left) and images of the anatomical location of RABV-traced neurons. The green arrowhead in S1 indicates a RABV-infected starter neuron. White arrowheads mark non-infected, electroporated neurons. White arrows mark RABV-traced neurons. Numbers identify cortical layers. Cl, contralateral; PO, posterior; Th, thalamus; VAL/VM, ventral-lateral/ventral-medial; VP, ventral-posterior. Scale bar, 250 μ m. **g**, IOC for brain regions in **f** for SRGAP2C mice relative to WT mice. $P = 2.54 \times 10^{-2}$ for M2 and $P = 1.56 \times 10^{-2}$ for contralateral S1. $*P < 0.05$, Kruskal–Wallis test. **h**, IOC for SRGAP2C mice relative to WT mice for cortical and subcortical inputs. $P = 3.33 \times 10^{-2}$ for cortical and $P = 0.98$ for subcortical. Bar graphs plotted as the mean \pm s.e.m. Open circles in the bar graphs indicate individual mice ($n = 10$ WT mice and $n = 7$ SRGAP2C mice), $*P < 0.05$, two-sided Mann–Whitney test. **i**, The fraction of inputs for all RABV-traced long-range inputs. CC, cortico–cortical; SC, subcortical.

digitally reconstructed, and the anatomical position of each traced neuron was mapped onto a reference atlas based on the Allen Institute Common Coordinate Framework¹³ (Fig. 1c–e, Extended Data Fig. 2a, Supplementary Video 1).

A large fraction of the traced neurons surrounded the starter neuron in ipsilateral S1 (Fig. 1f, Extended Data Fig. 2b, c; $n = 10$ for wild-type (WT) littermate controls and $n = 7$ for SRGAP2C mice). We consistently observed traced neurons in the secondary motor cortex (M2), the secondary somatosensory cortex (S2) and the S1 cortex contralateral to the starter neurons. We also traced presynaptic neurons from subcortical regions located almost exclusively in thalamic nuclei, such as ventral–anterior and lateral–medial, ventral–posterior and posterior nuclei (Fig. 1f–g, Extended Data Fig. 3a). Together, these five brain regions (ipsilateral S1, S2, M2, contralateral S1 cortex and ipsilateral thalamus) contained more than 95% ($95.8 \pm 1.5\%$ (mean \pm s.e.m.) for WT mice, $96.3\% \pm 1\%$ for SRGAP2C mice) of the traced neurons.

Increased connectivity in SRGAP2C mice

We next quantified the number of inputs received by WT or SRGAP2C-expressing layer 2/3 cortical PNs by calculating the index of connectivity (IOC), which is the number of traced neurons normalized by the number of

starter neurons. Long-range cortico–cortical feedback projections were significantly increased in SRGAP2C mice, but without a corresponding change in subcortical inputs (Fig. 1g–i). Connectivity originating in M2 was increased by equal amounts for both supragranular and infragranular layers, which maintained the relative proportion between supragranular and infragranular inputs (Fig. 2a, Extended Data Fig. 3b). By contrast, inputs from contralateral S1 onto SRGAP2C-expressing layer 2/3 PNs were more balanced between supragranular and infragranular layers compared with WT neurons (Fig. 2b, Extended Data Fig. 3c). For S2, there was a significant increase in inputs originating in layer 4 (Fig. 2c, Extended Data Fig. 3d), a projection that has recently been described as a non-canonical cortical feedback pathway between S2 and S1 (ref.¹⁴). The increased connectivity was not caused by differences in the cortical depth or the number of starter neurons between the two genotypes (Extended Data Fig. 4).

Focusing on local connectivity within S1, we noted a trend towards an increased IOC in SRGAP2C mice compared with WT mice (Fig. 2d, e). Local inputs onto layer 2/3 PNs consist of excitatory inputs from other PNs and inhibitory inputs from interneurons, the majority (approximately 80%) of which express either parvalbumin (PV; which marks fast-spiking large Basket cells) or somatostatin (SST; which marks dendrite-targeting interneurons). We performed post hoc immunofluorescence staining for PV and SST and quantified the IOC for these two subtypes (Fig. 2g, h). As PV-expressing and SST-expressing interneurons provide the majority of inhibitory inputs onto layer 2/3 PNs, RABV-traced cells that were negative for these markers were classed as excitatory neurons¹⁵. On the basis of previous work¹⁶, layer 1 neurons were classified as inhibitory irrespective of whether they were positive for PV or SST. No differences were observed for the IOC or the distribution of inhibitory interneurons (Fig. 2h, Extended Data Fig. 5e–h). By contrast, the fraction of RABV-traced excitatory neurons from granular (layer 4) and infragranular layers (layer 5/6) was significantly increased for SRGAP2C-expressing layer 2/3 PNs (Fig. 2h, i, Extended Data Fig. 5b–d). The spatial distribution of locally traced neurons was unchanged, which indicates that the increased inputs received by SRGAP2C-expressing layer 2/3 PNs originated from the same local cluster of neurons (Extended Data Fig. 5a, b). Together, these results show that SRGAP2C expression specifically increases the number of local excitatory feedforward inputs (in particular increased layer 4 to layer 2/3 connections) and long-range feedback inputs received by layer 2/3 PNs.

This selective increase in cortico–cortical feedforward and feedback connectivity may arise from changes in synaptic density localized to specific dendritic domains. Our previous work^{3,4} focused on an analysis of apical oblique dendrites, but did not examine whether SRGAP2C expression affects synaptic development in other dendritic compartments. Using our newly developed SRGAP2C mouse line, we found that spine density was increased in the apical oblique and distal tuft segment of adult SRGAP2C-expressing neurons compared with WT neurons, but we did not observe an increase in basal dendrites (Extended Data Fig. 6a–c). Spine sizes were similar between WT and SRGAP2C animals, which suggests that excitatory synapses reached maturation in SRGAP2C-expressing neurons after P65 (Extended Data Fig. 6d), which is similar to previously reported results^{3,4}.

Response reliability in SRGAP2C mice

Selectively increasing cortico–cortical connectivity may modify how layer 2/3 PNs process sensory information. To test this, we performed *in vivo* two-photon Ca²⁺ imaging in SRGAP2C mice crossed with *Thy1-GCaMP6f* (ref.¹⁷) and *Nex^{Cre}* mice and WT littermate controls ($n = 4$ WT mice and $n = 3$ SRGAP2C mice). This approach enabled us to image neuronal activity in layer 2/3 PNs ($n = 962$ neurons for WT and $n = 618$ for SRGAP2C) while ensuring that all imaged PNs express SRGAP2C (ref.¹⁸). We confirmed that this approach leads to an increase in synaptic density in distal and oblique dendritic domains of layer 2/3 cortical PNs, and

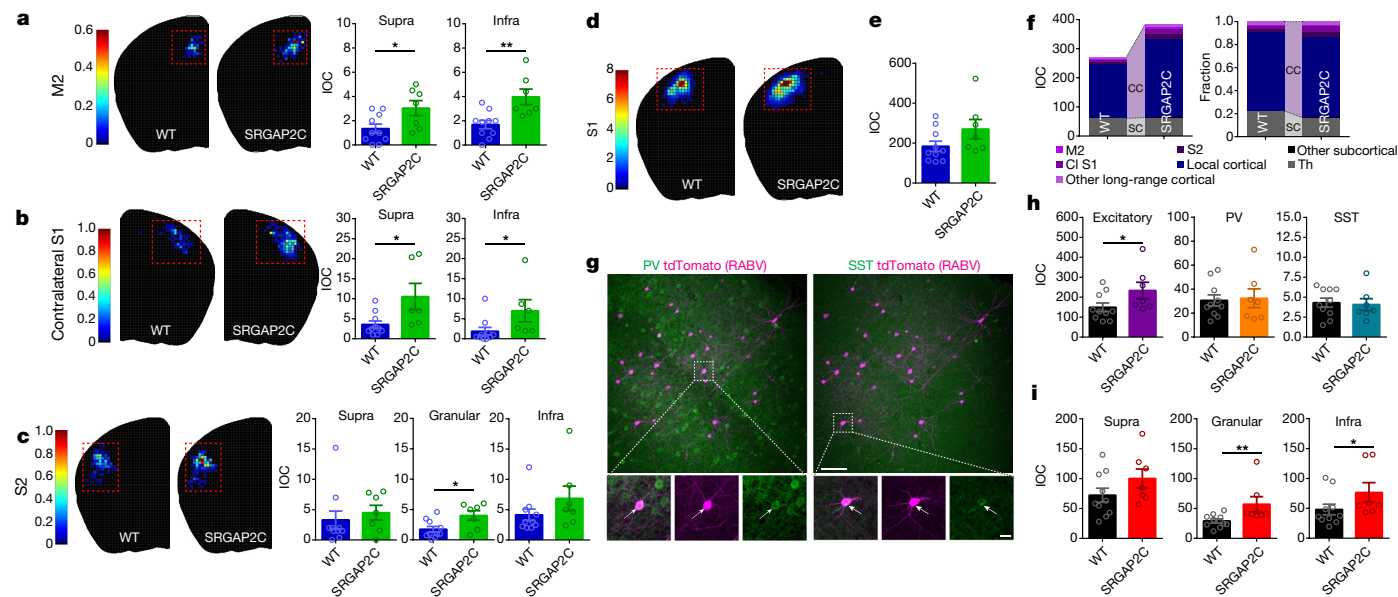


Fig. 2 | SRGAP2C expression increases cortical inputs onto layer 2/3 PN. **a–c**, Long-range cortical connectivity. IOC values for M2 (**a**), contralateral S1 (**b**) and S2 (**c**). Images on the left show distributions of traced neurons. Colours in the density plots indicate the IOC. Charts on the right indicate IOC values. For M2 (**a**), $P = 2.99 \times 10^{-2}$ for supragranular (Supra) and $P = 4.1 \times 10^{-3}$ for infragranular (Infra). For contralateral S1 (**b**), $P = 1.77 \times 10^{-2}$ for supragranular and $P = 1.39 \times 10^{-2}$ for infragranular. For S2 (**c**), $P = 2.63 \times 10^{-2}$ for granular. Two-sided Mann–Whitney test. **d–i**, Local connectivity (S1). **d**, The distribution of locally traced neurons in S1. Colours indicate the IOC. **e**, IOC for S1. $P = 0.109$, two-sided Mann–Whitney test. **f**, IOC (left) and fraction (right) for all RABV-traced inputs, including local cortical inputs originating in S1. **g**, Double

immunohistochemistry staining of the same RABV-traced brain section for PV (left) and SST (right). Bottom panels are higher magnification images of the areas indicated by dashed boxes above. Arrows indicate double-labelled neurons. Scale bar, 200 μ m (top) and 20 μ m (bottom). **h**, IOC values for excitatory, PV-positive and SST-positive RABV-traced neurons in S1. $P = 3.3 \times 10^{-2}$ for excitatory, two-sided Mann–Whitney test. **i**, IOC values for excitatory neurons in supragranular, granular and infragranular layers of S1. $P = 6.8 \times 10^{-3}$ and $P = 4.31 \times 10^{-2}$ for excitatory neurons in the granular and infragranular layers, respectively. Bar graphs plotted as the mean \pm s.e.m. Open circles in the bar graphs indicate individual mice ($n = 10$ WT mice and $n = 7$ SRGAP2C mice), $*P < 0.05$, $**P < 0.01$, two-sided Mann–Whitney test.

this was similar to the sparse manipulation of layer 2/3 PN (Extended Data Figs. 6 and 7a).

Whisker stimulation was performed on awake mice for 5 s per trial and repeated 24 times separated by a 25-s inter-trial interval (ITI) (Fig. 3a–c, Extended Data Fig. 7b). The following neuronal responses were recorded: time-locked to the onset of the stimulus (on); occurred during progression of the stimulus; time-locked to the offset of the stimulus (off); or negative (Extended Data Fig. 7d). Transients that were not time-locked to the onset or offset of the stimulus but occurred during the 5-s stimulus window (referred to as sustained responses) had overall longer response durations compared with on or off responses (Extended Data Fig. 7e).

We measured the response probability for each neuron by calculating the fraction of trials that led to a response (on, sustained or off), and we excluded neurons for which no responses were observed for any trials. Overall sensory-evoked response probabilities were low, with a long tail distribution in WT layer 2/3 PN (Extended Data Fig. 7c). By contrast, SRGAP2C-expressing neurons displayed a significantly higher response probability specifically for on responses, with a small but significant reduction in the response probability for sustained responses (Fig. 3d–f). Although the overall probability of negative responses was low, the probability of these responses was decreased for SRGAP2C-expressing neurons (Fig. 3g). In addition, the duration of sustained responses was significantly longer in SRGAP2C mice (Extended Data Fig. 7e–g). During the ITI, neuronal activity was reduced in SRGAP2C neurons with respect to both the number of transients and the transient amplitude (Fig. 3h, i; $P < 1 \times 10^{-4}$, Kolmogorov–Smirnov test), which was not explained by differences in behavioural activity such as whisking or grooming (Extended Data Fig. 7h, i). Together with a higher response probability for the onset of the stimulus, this led to activity patterns that were more restricted to sensory stimulus epochs, which resulted in an increase in response selectivity of SRGAP2C-expressing layer 2/3 PN (Fig. 3h).

The increased probability and selectivity of sensory-evoked neuronal responses suggests that SRGAP2C-expressing neurons encode sensory inputs in a more reliable manner. To determine this, we trained a linear support vector machine (SVM) to classify whether the stimulus was on or off for each time point. The accuracy of the classifier was significantly higher when using responses from SRGAP2C neurons, with a significant increase in correctly predicting the stimulus onset as well as more accurately predicting the continuation of the stimulus until stimulus offset (Extended Data Fig. 7j, k). Together, these results show that SRGAP2C expression in layer 2/3 PN improves the accuracy of sensory coding by increasing the response reliability and selectivity to whisker inputs.

An important feature that underlies the increased response probability is an increase in the ratio between evoked and spontaneous activity (Fig. 3d–i). To further investigate this, we analysed neuronal response properties by computing stimulus-triggered average fluorescence responses (Extended Data Figs. 8a, b and 9a). The fraction of neurons with positive evoked responses was larger in SRGAP2C mice, whereby 196 out of 581 (33.7%) of layer 2/3 PN showed increased activity following whisker stimulation in SRGAP2C mice compared with 222 out of 960 cells (23.1%) in WT mice. Conversely, only 14.5% showed a significant decreased evoked response in SRGAP2C mice following whisker stimulation compared with 27.7% in WT mice ($P < 0.05$, two-sample *t*-test). Changes in GCaMP6f fluorescence following sensory stimulation could reflect either actual changes in spiking frequency or changes in subthreshold events that indicate depolarization or hyperpolarization at the soma level¹⁹. To more accurately estimate whether the change in GCaMP6f fluorescence leads to changes in evoked spiking frequency, we applied spike deconvolution on GCaMP6f traces with sufficient signal-to-noise ratios. We again observed a significantly larger fraction of neurons with positive responses to whisker stimuli in the SRGAP2C mice, whereby 40 out of 72 (55.6%) of cells showed

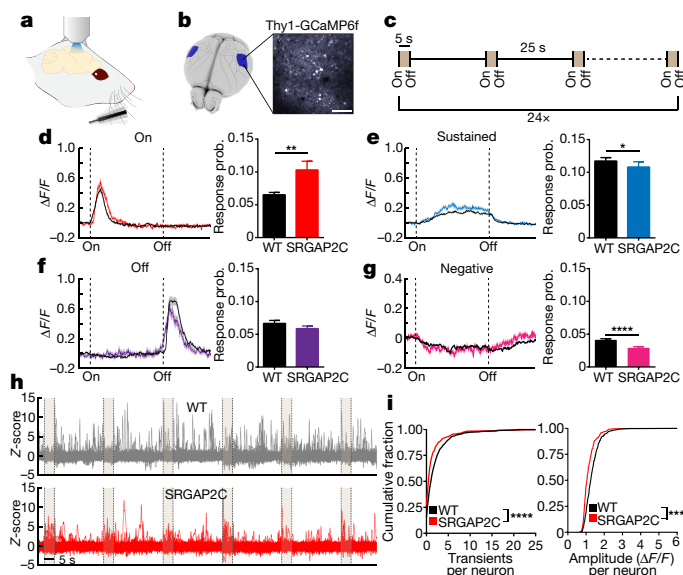


Fig. 3 | SRGAP2C increases the probability and selectivity of neuronal responses to sensory stimulation. **a**, Schematic of the experimental approach. **b**, In vivo two-photon Ca^{2+} imaging in S1 of WT or SRGAP2C mice during whisker stimulation. Scale bar, 100 μm . **c**, Whisker stimulation is repeated 24 times, with each stimulus lasting 5 s and a 25 s interval between stimuli. **d–g**, Left, average calcium traces ($\Delta F/F$) for on (**d**), sustained (**e**), off (**f**) and negative (**g**) response types. Shaded area indicates s.e.m. Right, response probability (Response prob.) expressed as the fraction of stimuli leading to a response. $P = 6.4 \times 10^{-3}$ for on (**d**), $P = 4.31 \times 10^{-2}$ for sustained (**e**) and $P = 3.21 \times 10^{-1}$ for off (**f**). Bar graphs plotted as the mean \pm s.e.m. * $P < 0.05$, ** $P < 0.01$, **** $P < 0.0001$, two-sided Mann–Whitney test. **h**, A total of 150 randomly chosen Z-scored example traces for WT (top) and SRGAP2C (bottom) mice showing activity during six consecutive stimuli (shaded) and the corresponding ITIs. **i**, Cumulative probability distribution of Ca^{2+} transient number (left) and amplitude (right) during ITIs. **** $P < 0.0001$, Kolmogorov–Smirnov test ($n = 580$ neurons for WT and $n = 277$ neurons for SRGAP2C).

a significant decrease in response, whereas 20.8% had a significant increase in response ($P < 0.05$, two-sample t -test). By contrast, for WT mice (Extended Data Fig. 8b), 129 out of 377 (34.2%) of cells had a significant decrease in responses, whereas 8.8% had a significant increase in response ($P < 0.05$, two-sample t -test). This difference was robust against the choice of different thresholds of signal-to-noise ratio for cell selection (Extended Data Fig. 9b). Together, this analysis revealed that SRGAP2C expression in PN significantly modifies the neural population response dynamics by increasing the ratio between evoked responses and spontaneous activity (Extended Data Fig. 8c).

Next, we used a computational modelling approach to test the hypothesis that increased cortico–cortical connectivity is sufficient to drive some of the changes in sensory-evoked response properties. We focused on the increased connectivity between layer 4 and layer 2/3 PNs because of the well-documented effect this feedforward connection has on driving layer 2/3 PNs responses to whisker stimulation²⁰. We developed a computational model of the layer 2/3 local network with input from layer 4 (Extended Data Fig. 8d). The model considered only the total number of connections and was agnostic on whether the increase in connections originated from an increased number of presynaptic neurons or from an increased number of connections per connected pair. In a broad parameter regime, an increase in strength of these two connections (thick black lines for SRGAP2C in Extended Data Fig. 8d) led to increases in the mean spiking activity of layer 2/3 PNs with respect to the input strength (Extended Data Fig. 8e, f, h). Accordingly, the ratio of evoked-to-spontaneous excitatory mean activity monotonically increased with an increase in the strength of the two connections (Extended Data Fig. 8g). Thus, both the model

and the data show that spontaneous and sensory-evoked mean activity, as well as the ratio of evoked-to-spontaneous mean activity, are all increased in SRGAP2C mice. Parameter sets that reproduced these effects had excitatory-to-excitatory connections as the weakest among the four sets of connections strengths, whereas inhibitory-to-inhibitory connections were the strongest.

We also modelled the distribution of activity across the excitatory neuronal population. In the model (Extended Data Fig. 8i), as in the data (Extended Data Fig. 8c), both WT and SRGAP2C layer 2/3 PN populations included neurons that increased and decreased their activity in response to a stimulus (stimulation of layer 4 activity) relative to spontaneous activity. Moreover, SRGAP2C mice had a higher fraction of neurons that exhibited increased activity in response to activation of layer 4 (stimulus). The standard deviation of the response distribution also increased with the strength of the stimulus and the strength of the connections (Extended Data Figs. 8j and 9d–f), a result consistent with the data (Extended Data Fig. 9c). This effect depended on the variability in both the recurrent weights and the presynaptic inputs from layer 4. Our model demonstrates that the observed increase in excitatory layer 4 to layer 2/3 PN connections is sufficient to account for some of the key observed changes in the response properties in layer 2/3 PNs in SRGAP2C mice relative to WT mice.

Sensory discrimination in SRGAP2C mice

We next evaluated whether increased feedforward and feedback cortico–cortical connectivity together with improved sensory coding accuracy in SRGAP2C mice affects behavioural performance. We tested the ability of WT littermate control and *Nex^{cre}-SRGAP2C* mice to learn a whisker-based texture-discrimination task that has previously been shown to rely on cortical processing^{21–23}. Mice were trained in a two-alternative forced-choice task to discriminate two different rough textures (Fig. 4a, b, Supplementary Video 2), which is a more difficult task than a smooth versus rough texture-discrimination task²³. Performance was whisker-dependent and improved over sessions (50 days) for both WT and SRGAP2C mice (Fig. 4c, Extended Data Fig. 10a, b; $n = 20$ for WT mice and $n = 18$ for SRGAP2C mice, pooled from two independent cohorts).

As a group, SRGAP2C mice displayed an increased learning rate, which was evident from a difference in the slope of the performance curve (Fig. 4c). Owing to the difficulty of the task, each group consisted of learners (>75% correct) and non-learners (Fig. 4d). SRGAP2C mice were more likely to learn the task than WT mice (Fig. 4e), an effect that was consistent for two independently tested cohorts (cohort 1 learners: 62.5% for WT mice and 88.9% for SRGAP2C mice; cohort 2 learners: 58.3% for WT mice and 90.9% for SRGAP2C mice). These results were not explained by the difference in the number of sessions or trials that the mice performed during the training stage or by the difference in the number of sessions or trials run for pre-training (Extended Data Fig. 10c). There was no difference in overall water intake, which suggests that there was no increased motivation due to potential higher thirst levels (Extended Data Fig. 10d).

We wondered whether the improved learning performance of SRGAP2C mice was due to an enhanced ability to perceive texture differences. To assess this, we analysed the lick responses of naive and expert learners (Extended Data Fig. 10e–i). Naive mice extensively licked the port even before the texture was within reach of the whiskers (sampling window in Extended Data Fig. 10e). By contrast, expert mice restricted their licking to the sampling window. Although we did not observe any difference between naive WT mice and SRGAP2C mice, the expert SRGAP2C mice increased their lick frequency earlier in the sampling window (Extended Data Fig. 10g, h). This earlier lick response corresponded with a trend for SRGAP2C mice to respond with higher accuracy earlier in the sampling window (Extended Data Fig. 10i). To further investigate this result, we analysed behavioural performance during the pre-training phase. Here, mice are required to alternate their lick responses between left and right while they are presented with the corresponding texture. During this

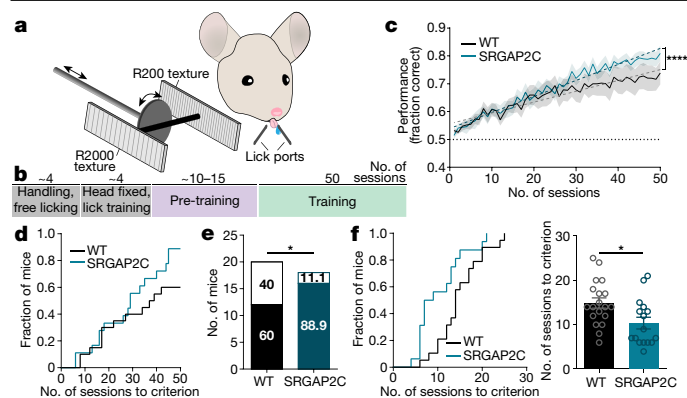


Fig. 4 | Humanized SRGAP2C mice display an increased ability to learn a texture-discrimination task. **a, b,** Schematics of the whisker-based texture-discrimination task. The distance between the laser cut grooves for the R200 and R2000 textures is 200 and 2,000 μm , respectively. **c,** Behavioural performance shown as the fraction of correct trials over sessions of training (one session per day). The shaded area indicates the s.e.m. Linear regression is indicated by dashed lines. The dotted horizontal line indicates chance level performance (50% correct). Linear regression, slope WT = 0.0039, slope SRGAP2C = 0.0057. **** $P < 0.0001$, linear regression F -test. **d,** Cumulative histogram of the number of sessions required to achieve the learning criterion (75% correct). **e,** The number of learners (mice that reached 75% correct responses) and non-learners (mice that never reached 75% correct responses). Numbers in bar graphs indicate the percentage of total number of mice tested. $P = 0.043$, chi-square test. **f,** Left, cumulative histogram of the number of sessions required to achieve the learning criterion during pre-training (75% correct responses). Right, number of sessions to reach the criterion. $P = 0.0135$, two-sided Mann–Whitney test. Bar graphs plotted as the mean \pm s.e.m. Open circles in the bar graphs indicate individual mice ($n = 19$ WT mice and $n = 16$ SRGAP2C mice), * $P < 0.05$.

forced-alternation phase, mice can learn the rule of the task independent of texture information (that is, even without presentation of the textures), and the mice can learn the alternation rule by keeping track of which side the reward was presented on the previous trial. However, given that the textures provide a clue about which side the reward will be located, the textures provide additional context for mice to learn the rule of the task during the pre-training period. Interestingly, SRGAP2C mice required significantly fewer sessions than WT mice to reach criterion during pre-training (Fig. 4f).

Discussion

The results presented in this study demonstrate that expression of the human-specific gene duplication *SRGAP2C* in cortical PNs alters cortical circuit connectivity by increasing the number of local and long-range cortical inputs received by layer 2/3 PNs. Moreover, it increases the probability of sensory-evoked responses by layer 2/3 PNs and enhances sensory learning in a cortex-dependent texture-discrimination task.

To correctly perform this texture-discrimination task, mice must learn to discriminate two textures using their whiskers and to learn an abstract association between each texture and the correct lick port for reward. Strikingly, only 60% of WT mice learned this task after 50 training sessions, which illustrates that this behaviour is cognitively demanding for WT mice. Increased cortico–cortical connectivity and increased reliability of sensory coding may offer one potential explanation for this improvement in behavioural performance in SRGAP2C mice, but several other possible contributing factors could be involved. These include more synchronous dendritic and/or somatic inhibition, which has recently been shown to shape responses selectivity in multiple circuits^{24,25}. Furthermore, it remains to be determined how local and long-range cortical projections work together to facilitate increased sensory learning. One possibility is that increased local connectivity from layer 4 enhances sensory coding in S1, which is what our modelling

data suggest. This may enable a more reliable detection of subtle differences between textures. In turn, increased long-range cortico–cortical connectivity, which might facilitate more effective communication between cortical regions such as M2 and S1, could subsequently propagate this more reliable signal to other cortical regions for a more effective association of the texture with appropriate behavioural output.

In summary, we propose that our results identified a new substrate for human brain evolution. That is, the emergence of *SRGAP2C* approximately 2–3 million years ago at the birth of the *Homo* lineage—but before the main phase of brain volume increase¹—led to increased cortico–cortical connectivity, enhanced sensory coding by layer 2/3 PNs and improved behavioural performance, all of which are required to solve complex cognitive tasks that involve associative learning.

Online content

Any methods, additional references, Nature Research reporting summaries, source data, extended data, supplementary information, acknowledgements, peer review information; details of author contributions and competing interests; and statements of data and code availability are available at <https://doi.org/10.1038/s41586-021-04039-4>.

- Dennis, M. Y. et al. The evolution and population diversity of human-specific segmental duplications. *Nat. Ecol. Evol.* **1**, 0069 (2017).
- Ponce de León, M. S. et al. The primitive brain of early *Homo*. *Science* **372**, 165–171 (2021).
- Charrier, C. et al. Inhibition of *SRGAP2* function by its human-specific paralogs induces neoteny during spine maturation. *Cell* **149**, 923–935 (2012).
- Fossati, M. et al. *SRGAP2* and its human-specific paralog co-regulate the development of excitatory and inhibitory synapses. *Neuron* **91**, 356–369 (2016).
- Schmidt, E. R. E., Kupferman, J. V., Stackmann, M. & Polleux, F. The human-specific paralogs *SRGAP2B* and *SRGAP2C* differentially modulate *SRGAP2A*-dependent synaptic development. *Sci. Rep.* **9**, 18692 (2019).
- Sudmant, P. H. et al. Diversity of human copy number variation and multicopy genes. *Science* **330**, 641–646 (2010).
- Fortna, A. et al. Lineage-specific gene duplication and loss in human and great ape evolution. *PLoS Biol.* **2**, E207 (2004).
- Sporny, M. et al. Structural history of human *SRGAP2* proteins. *Mol. Biol. Evol.* **34**, 1463–1478 (2017).
- Benavides-Piccione, R., Ballesteros-Yáñez, I., DeFelipe, J. & Yuste, R. Cortical area and species differences in dendritic spine morphology. *J. Neurocytol.* **31**, 337–346 (2002).
- Elston, G. N., Benavides-Piccione, R. & DeFelipe, J. The pyramidal cell in cognition: a comparative study in human and monkey. *J. Neurosci.* **21**, RC163 (2001).
- Reardon, T. R. et al. Rabies virus CVS-N2c δ G strain enhances retrograde synaptic transfer and neuronal viability. *Neuron* **89**, 711–724 (2016).
- Wickersham, I. R., Finke, S., Conzelmann, K. K. & Callaway, E. M. Retrograde neuronal tracing with a deletion-mutant rabies virus. *Nat. Methods* **4**, 47–49 (2007).
- Allen Mouse Common Coordinate Framework. Technical White Paper (Allen Institute for Brain Science, 2015).
- Minamisawa, G., Kwon, S. E., Chev e, M., Brown, S. P. & O’Connor, D. H. A non-canonical feedback circuit for rapid interactions between somatosensory cortices. *Cell Rep.* **23**, 2718–2731.e6 (2018).
- Tremblay, R., Lee, S. & Rudy, B. GABAergic interneurons in the neocortex: from cellular properties to circuits. *Neuron* **91**, 260–292 (2016).
- Genescu, I. & Gareil, S. Being superficial: a developmental viewpoint on cortical layer 1 wiring. *Curr. Opin. Neurobiol.* **66**, 125–134 (2021).
- Dana, H. et al. *Thy1-GCaMP6* transgenic mice for neuronal population imaging in vivo. *PLoS ONE* **9**, e108697 (2014).
- Goebbels, S. et al. Genetic targeting of principal neurons in neocortex and hippocampus of *NEX-Cre* mice. *Genesis* **44**, 611–621 (2006).
- Grienberger, C. & Konnerth, A. Imaging calcium in neurons. *Neuron* **73**, 862–885 (2012).
- Petersen, C. C. H. Sensorimotor processing in the rodent barrel cortex. *Nat. Rev. Neurosci.* **20**, 533–546 (2019).
- Guic-Robles, E., Jenkins, W. M. & Bravo, H. Vibrissal roughness discrimination is barrel cortex-dependent. *Behav. Brain Res.* **48**, 145–152 (1992).
- Manita, S. et al. A top-down cortical circuit for accurate sensory perception. *Neuron* **86**, 1304–1316 (2015).
- Park, J. M. et al. Deep and superficial layers of the primary somatosensory cortex are critical for whisker-based texture discrimination in mice. Preprint at *bioRxiv* <https://doi.org/10.1101/2020.08.12.245381> (2020).
- Geiller, T. et al. Large-scale 3D two-photon imaging of molecularly identified CA1 interneuron dynamics in behaving mice. *Neuron* **108**, 968–983.e9 (2020).
- Rossi, L. F., Harris, K. D. & Carandini, M. Spatial connectivity matches direction selectivity in visual cortex. *Nature* **588**, 648–652 (2020).

Publisher’s note Springer Nature remains neutral with regard to jurisdictional claims in published maps and institutional affiliations.

  The Author(s), under exclusive licence to Springer Nature Limited 2021, corrected publication 2022

Methods

Mice

All animals were handled according to protocols approved by the institutional animal care and use committee (IACUC) at Columbia University. All mice used in experiments were adults (>P65), heterozygous for the indicated transgenes and were maintained on a 12-h light/dark cycle at 20–22 °C and humidity between 30 and 70%. *Nex^{cre}* (*NeuroD6^{tm1(cre)Kan}*) mice¹⁸ were obtained from The Jackson Laboratory. These mice have induced recombination in dorsal telencephalic-derived postmitotic neurons that give rise to all PNs throughout the cortex, the hippocampus and the amygdala but not in astrocytes, interneurons or microglial cells in these structures. *Thy1-GCaMP6f* mice¹⁷ were obtained from The Jackson Laboratory (C57BL/6J-Tg(Thy1-GCaMP6f)GP5.17Dkim/J) and stochastically express GCaMP6f in a subset of excitatory PNs in various brain regions, including the cortex and the hippocampus.

Conditional SRGAP2C-expressing mice were generated using homologous recombination in C57BL/6J mouse embryonic stem (ES) cells (see Extended Data Fig. 1 for details) in collaboration with genOway. A targeting vector containing a CAG promoter, *SRGAP2C*-3×HA cDNA, rabbit-globin poly-A, a *loxP*-STOP-*loxP* and neomycin selection cassette, and homology arms consisting of sequences between exon 1 and exon 2 of the *Rosa26* locus was constructed. In addition, diphtheria toxin A cDNA was placed downstream of the 3' homology arm for the negative selection of non-recombined ES cell clones. Southern blot analysis was used to confirm homologous recombination of the targeting vector in ES cell clones. Recombined ES cell clones were injected into C57BL/6J blastocysts and re-implanted into OF1 pseudo-pregnant females to generate chimeric males. Male chimeras were subsequently bred with WT C57BL/6J females to generate an F₁ population of SRGAP2C mice. Heterozygous mice (*Rosa26^{SRGAP2C}*(F/+)) were confirmed carriers of the transgene by genomic PCR and Southern blot analysis (Extended Data Fig. 1). WT and SRGAP2C alleles were identified by PCR of genomic DNA using the following primers: 5'-CAATACCTTCTGGGAGTCT-3' and 5'-CTGCATAAACCCAGATGAC-3' for detection of the WT allele; and 5'-CATGGGGATATGGCTTC-3' and 5'-GGAACATCGTATGGTAAGCG-3' for detecting the presence of *Rosa26*-targeted SRGAP2C. For the in utero electroporation experiments, mice were crossed once with the outbred strain 129S2/SvPasCrl mice (obtained from Charles River) to produce F₁ hybrid females used to generate timed-pregnant females by crossing with *Rosa26^{SRGAP2C}*(F/+) heterozygous males (on pure C57BL/6J background). In this study, we refer to SRGAP2C mice as animals that are heterozygous for the *Rosa26^{SRGAP2C}*(F/+) allele.

Western blotting

Cre-dependent expression of SRGAP2C-HA protein was analysed by crossing SRGAP2C mice with *Nex^{cre}* mice¹⁸ to induce expression of SRGAP2C in all excitatory forebrain neurons. Cortical hemispheres were dissected and homogenized in ice-cold homogenization buffer (N-PER neuronal protein extraction reagent (ThermoFisher Scientific) with complete protease inhibitor cocktail (Roche), 10 μM MG-132 (Sigma-Aldrich) and Benzamide (EMD Millipore)) using a disposable Biomasher II (Kimble Chase). After homogenization, samples were incubated for 30 min at 4 °C in homogenization buffer and subsequently centrifuged at 10,000g for 30 min in a cooling centrifuge at 4 °C. Samples were prepared in Laemmli buffer (Bio-Rad) containing 10% 2-mercaptoethanol and boiled at 95 °C for 5 min. Using SDS-PAGE, proteins were separated and then transferred to a polyvinylidene difluoride membrane (Immobilon-FL, EMD Millipore). Western blotting was performed using anti-HA primary (1:1,000; anti-HA.11901513, BioLegend) and anti-actin (1:5,000; MAB1501, Millipore) antibodies together with goat-anti-mouse IgG conjugated to IRDye 800CW (1:10,000; Li-Cor) and goat-anti-mouse IgG conjugated to IRDye 680RD (1:40,000). Imaging of immunoblots was performed using an Odyssey CLx imaging system (Li-Cor).

DNA constructs

The BHTG construct was generated by subcloning mTagBFP-3×HA, histone-GFP, TVA66T and the N2c glycoprotein together with 2A self-cleaving peptide sequences (see Fig. 1b for details) in between *NheI* and *AscI* cloning sites of the pAAV-Efla-DIO eNpHR 3.0-eYFP plasmid (Addgene plasmid 26966) using Gibson assembly cloning. pCAG-Cre was generated in the Polleux laboratory as previously described²⁶.

IUCE experiments

IUCE was performed at embryonic day 15.5 (E15.5) on isoflurane-anaesthetized timed-pregnant SRGAP2C or control female mice as previously described²⁷, but with the following modifications. Endotoxin-free DNA containing 1 μg μl⁻¹ BHTG plasmid and 10–20 ng μl⁻¹ Cre plasmid, 1 μg μl⁻¹ mRuby-Cre plasmid (for Extended Data Fig. 1), or a Flp-dependent version of the BHTG plasmid with 10–20 ng μl⁻¹ FlpO plasmid (for Extended Data Fig. 7a), was injected into the ventricles of E15.5 embryos using a heat-pulled capillary. Electroporation was performed by applying 5 pulses of 42 V for 50 ms with 500-ms intervals using a 3-mm diameter platinum tweezer electrode (Nepa Gene) and a square wave electroporator (ECM 830, BTX). After placing embryos back into the abdominal cavity, the incision was closed using sutures and the mouse was allowed to recover on a heating plate.

Virus injection

Adult mice were anaesthetized using isoflurane and placed in a stereotaxic frame (Stoelting). A small burr hole was drilled over the barrel field of the primary sensory cortex (1.3 mm posterior and 3 mm lateral to Bregma²⁸) using a high-speed dental drill. A glass pipette (Drummond Scientific) was heat-pulled (Narishige PC-10) to produce a tip of approximately 10 μm in diameter. It was then filled with viral vector solution containing CVS-N2c^{Δg} [EnvA] RABV-tdTomato and lowered into the brain to a depth of 200–300 μm. Virus was subsequently injected at bouts of 25 nl at 2 nl s⁻¹ with a 20-s interval until a total volume of 400–500 nl was injected. The glass injection pipette was left for 2 min after the injection was completed, after which it was slowly removed. The skin was closed using sutures and the mouse was allowed to recover on a heating plate. Mice were left for 7 days to allow enough time for RABV-tdTomato to reach sufficient levels of expression in both starter neurons and presynaptic inputs.

Sparse monosynaptic RABV tracing and whole brain reconstruction

Tissue preparation. After 7 days of RABV tracing, mice were anaesthetized with isoflurane, and intracardiac perfusion was performed using 4% paraformaldehyde (Electron Microscopy Sciences) in PBS. Brains were isolated and incubated overnight in a 4% paraformaldehyde in PBS solution at 4 °C. The following day, brains were washed in PBS and sectioned along the coronal plane at 100 μm using a vibrating microtome (Leica VT1200S). Approximately 100 sections were collected spanning the most rostral part of the cortex to the cerebellum. Sections were stained using Hoechst 33258 (Sigma-Aldrich) and subsequently mounted on glass slides in Fluoromount-G aqueous mounting medium (ThermoFisher Scientific).

Image acquisition. Sections were first imaged on a Nikon SMZ18 stereomicroscope with an automatic stage using a SHR Plan Apo ×1 objective at a zoom magnification of ×4. Stitching was performed directly after imaging using Nikon NIS-Elements software. Sections containing cells positive for both tdTomato and histone-GFP were subsequently imaged by collecting z-stacks on a Nikon A1 confocal microscope using a ×1 Plan Apo NA 0.45 objective (Nikon) for identification of RABV starter neurons, which we identified by the co-expression of hGFP and tdTomato. Additional confirmation of starter neurons was done by imaging these neurons again using a ×40 Plan Apo NA 0.95 (Nikon) objective.

Section alignment and registration to atlas. Imaged sections were aligned using rigid body alignment in StackReg (ImageJ plugin), and manual adjustments were made using Adobe Photoshop when necessary. Neurons were subsequently counted and annotated using a Cell Counter plugin (Fiji-ImageJ), after which sections and coordinates were imported into 3ds Max (Autodesk). Landmarks were then manually placed at multiple anatomical locations (113 anatomical landmarks) corresponding to landmarks we assigned to a three-dimensional mouse brain atlas imported from the Allen Brain Institute (Common Coordinate Framework 3). Landmarks were placed at anatomical regions that were easily identified in imaged sections, such as the first section containing the hippocampus or the first section where the corpus callosum forms a continuous bundle. In addition, a single landmark indicating the point at which both cortical hemispheres meet was assigned to each section (designated as the midline landmark). Using these assigned landmarks, together with custom-written scripts in MAXScript, the following tasks were performed: (1) the section stack was resized to match the reference brain size; (2) based on the midline landmark, each section was aligned along the dorsal–ventral axis of the reference brain; and (3) using anatomical landmarks, each neuron was assigned to the corresponding location in the reference brain. Finally, to assign proper cortical depth to each neuron, the pial surface was traced and reconstructed for each section, and the distance to the pial surface for each neuron was measured along the line that perpendicularly intersects the pial surface. Neurons were colour coded according to their assigned brain region or their calculated cortical depth to manually confirm proper alignment to the reference brain. Finally, the three-dimensional position and assigned brain region for each neuron was exported for subsequent analysis.

Identification of interneurons. Tissue sections were washed in PBS and subsequently blocked overnight at 4 °C in blocking buffer (PBS containing 1% Triton X-100 (Sigma-Aldrich) and 5% goat serum (Gibco)). The following day, sections were washed 3 times for 1 h in PBS containing 0.5% Triton X-100. Next, sections were incubated with primary antibody in PBS containing 0.5% Triton X-100 and 0.5% goat serum for 4 days at 4 °C. Sections were then washed 3 times for 1 h in PBS containing 0.5% Triton X-100, after which they were incubated with secondary antibodies conjugated to Alexa Fluor-488, -546 and -647 of appropriate species (1:500, ThermoFisher Scientific). After several washes in PBS, sections were mounted on glass slides with Fluoromount-G. The z-stacks were collected by imaging on a Nikon A1 confocal microscope using a $\times 10$ Plan Apo NA 0.45 objective (Nikon) to confirm neuronal identity for RABV-traced neurons. Primary antibodies used were mouse anti-HA (1:1,000; anti-HA.11, BioLegend), rat anti-SST (1:100; MAB354, Millipore), guinea pig anti-PV (1:200; 195004, Synaptic Systems) and rabbit anti-DsRed (1:500; 632496, Takara Bio).

Data analysis. The IOC was calculated for each animal by dividing the number of traced neurons by the number of starter neurons. Average IOC density maps showing the distribution of traced neurons across the brain were generated using Matlab (Mathworks) by producing IOC density maps per animal and subsequently combining these maps to calculate an average IOC density map per genotype. For density maps showing the distribution of neurons relative to their closest starter neuron, we determined, per animal, the closest starter neuron for each traced neuron in the primary sensory cortex (S1). We then calculated the relative medial–lateral and rostral–caudal position of each traced neuron with respect to the closest starter neuron. The majority of traced neurons in S1 form a dense cloud closely around the starter neuron. However, this approach may misclassify which starter neuron belongs to which traced neurons when multiple starter neurons are in close proximity to each other. Differences in the distance between starter neurons in a single brain for WT mice and SRGAP2C mice could

therefore obscure a potential change in the distribution of traced neurons between WT mice and SRGAP2C mice. We therefore analysed the minimum distance between starter neurons for brains with more than one starter neuron. There was no difference in the distribution of starter neurons between WT mice and SRGAP2C mice (distance from starter neuron to nearest other starter neuron: $300.4 \pm 55.92 \mu\text{m}$ (mean \pm s.e.m.) for WT and $357.1 \pm 74.19 \mu\text{m}$ for SRGAP2C). Furthermore, when we analysed brains with only 1 starter neuron ($n = 3$ for WT and $n = 2$ SRGAP2C) we similarly did not observe a difference in the spatial distribution of traced neurons (data not shown).

Dendritic spine analysis

Dendritic spine quantification. Tissue sections were washed in PBS and subsequently blocked for 3 h at room temperature in blocking buffer (PBS containing 0.2% Triton X-100 (Sigma-Aldrich) and 5% goat serum (Gibco)). Next, sections were incubated with primary antibody in PBS containing 0.2% Triton X-100 and 5% goat serum overnight at 4 °C. The next day, sections were washed 3 times for 30 min in PBS containing 0.2% Triton X-100. Sections were then incubated for 1 h with secondary antibodies conjugated to Alex Fluor-546 or 647 of appropriate species (1:500, ThermoFisher Scientific). After several washes in PBS, sections were mounted on glass slides using Fluoromount-G. Imaging of dendritic spines was performed using a Nikon A1 confocal microscope. First, low-magnification z-stack images were collected using a $\times 20$ Plan Apo NA 0.75 objective (Nikon) to visualize the entire dendritic tree of optically isolated neurons. Next, appropriate terminal branches were selected for distal, apical oblique and basal dendritic segments, for which we collected z-stack images using a $\times 100$ H-TIRF, NA 1.49 objective (Nikon).

Data analysis. Nikon NIS-Elements was used to generate a z-stack maximum intensity projection of selected dendritic branches. We then quantified spine density and head size by tracing the dendritic segment to measure the dendritic length and drawing regions of interest (ROIs) around the spine head as visualized by the mTagBFP-HA filler signal.

Two-photon calcium imaging

Surgery and image acquisition. Adult mice were anaesthetized using isoflurane and injected with buprenorphine (0.1 mg kg^{-1} body weight), after which the dorsal skull was exposed and cleaned with a razor blade. A craniotomy was performed, and a glass window was placed over the barrel field of the primary sensory cortex. The window was glued in place using cyanoacrylate glue, after which a custom head plate was secured onto the skull using both cyanoacrylate glue and dental acrylic cement. Mice were allowed to recover for a minimum of 7 days, after which imaging in awake mice ($n = 4$ WT and $n = 3$ SRGAP2C) was conducted on a Bergamo II two-photon microscope (Thorlabs), running ThorImage LS and Thorsync, using a $\times 16$ 0.8 NA objective (Nikon) and 920-nm wavelength Ti-sapphire laser (Coherent). Imaging was performed 150–250 μm below the pial surface at 30 Hz and 512×512 pixels covering $830 \times 830 \mu\text{m}$. For whisker stimulation trials, a transparent acrylic rod was placed next to the right whisker pad at a fixed distance of 2 mm. Every stimulus trial consisted of a 10-s pre-stimulus, a 5-s stimulus and a 15-s post-stimulus period. Six trials were grouped into a single run, separated by 25-s intertrial interval, and 4 runs were performed per session (total of 24 stimuli). Whisker stimuli were applied by vibrating the bar at 25 Hz, a speed of more than 100 mm s^{-1} , and an amplitude of more than 1 mm. To identify the responding region in the barrel field of the primary sensory cortex contralateral to the stimulated whisker pad, we first performed a wide-field imaging experiment in which the entire region under the cranial window was imaged during multiple stimulus trials. The haemodynamic component was calculated and the neural signal was isolated as previously described²⁹. Subsequent two-photon imaging was performed on two to three non-overlapping

fields of view (FOVs) per mouse within the centre of the activated area. Activity of the animal during imaging was monitored using an infrared camera.

Image processing and analysis. Non-rigid motion correction of acquired images was performed using NoRMCorre as previously described³⁰. ROIs were manually drawn over soma of individual neurons. All subsequent analyses were done using custom-written Matlab code, which is available upon request. Time courses were calculated as the mean of all pixels within the ROI. The neuropil signal was estimated by dilating neuronal ROIs by 4 pixels to form a ring-shaped neuropil ROI around the soma of each neuron. To remove neuropil contamination, we subtracted the change in fluorescence ($\Delta F/F$) neuropil signal from the $\Delta F/F$ neuronal signal. To avoid subtraction of a signal not considered neuropil contamination, we excluded pixels in the neuropil ROI that contained transients exceeding two times the standard deviation of the difference between the neuropil and neuronal signals as previously described³¹. To identify the response type per stimulus for each neuron, we aligned all time courses to their respective stimulus onset and performed K -means clustering with 60 clusters and correlation as the distance metric. Common time-courses were identified by running K -means 200 times with random initialization. The resulting outputs of the repeated K -means were clustered a final time to obtain a set of representative responses. Clusters with responses for which the onset time was time-locked with the start or end of the whisker stimulus were determined to be an on or off type of response, respectively. Those occurring during the duration of stimulus were grouped as sustained-type responses. Neuronal responses were subsequently assigned to a cluster by evaluating the Pearson's correlation between the time course and each basis time-course. The highest correlation value greater than 0.4 was determined to be the representative time course. The duration of sustained responses was calculated as the time at which the Z -scored time courses was greater than 1. To characterize activity during the ITI, transients were identified by finding the local maxima during ITI periods. Peaks were constrained to having widths of at least two frames, a minimum $\Delta F/F$ of 0.5 and a relative increase in $\Delta F/F$ of 6 times the standard deviation compared with the preceding local minimum. A frame-to-frame sliding window correlation analysis of webcam images was done to determine periods and duration of active behaviour such as whisking or grooming.

SVM classification

Time courses for all neurons were Z -scored, after which for each FOV, a random number of ten neurons were selected to train a linear SVM to classify between the presence (on) and absence (off) of a whisker stimulus. For each FOV, the SVM was performed 50 times, each time with a new randomly selected group of 10 neurons. Each iteration was performed with 5-fold cross validation using 80% of time points for training and the remaining 20% for testing. Accuracy was calculated as the average across all 50 iterations. We repeated this procedure by progressively increasing the number of neurons per FOV used for the SVM by five. To calculate accuracy of the SVM across time, we calculated the average accuracy for each time point across all 24 stimuli. This generated an average accuracy value for each time point of the time course. We grouped these results for WT and SRGAP2C FOVs to generate an average accuracy across genotypes and normalized the results to the maximum (set to 1) and minimum (set to 0) values. All SVM analyses were performed using custom written Matlab code (Mathworks).

Stimulus-triggered responses

To compute the stimulus-triggered response of each neuron, we first subtracted the raw neuropil signal F_n from the raw ROI signal F_r using a neuropil factor of $\alpha = 0.7$, which is consistent with a previous study that used *Thy1-GCaMP6* mice¹⁷, such that the signal considered was

$F_s = F_r - \alpha F_n$. Then we computed $\Delta F/F_0$ by estimating F_0 as the lower fifth percentile of the whole trace F_s and then computing $\frac{\Delta F}{F_0} = \frac{F_s - F_0}{F_0}$. For every stimulus repetition, we considered a period starting from 5 s before the stimulus onset and ending 15 s after the stimulus offset for a total period of 25 s, with a stimulus duration of 5 s. We then averaged the corresponding fluorescence traces across all repetitions to obtain a stimulus-triggered fluorescence average for each neuron. For visualization purposes in Extended Data Fig. 8a, we first Z -scored the traces and then subtracted the average Z -score activity during the 5 s before the stimulus. We performed a paired t -test between the average activity during 5 s before the stimulus and 5 s of stimulation and obtained a P value, P_i , for each neuron. We then sorted the neurons according to their P values and the sign of their responses (depending on whether the activity increased or decreased from spontaneous to evoked) such that neurons at the top (bottom) of the colour map corresponded to those with the more robust increase (decrease) in activity.

We performed spike deconvolution using the method MLspike³². We used as a calcium indicator time constant $\tau = 0.167$ s, which was consistent with the one reported for GCaMP6f (ref. ¹⁷). We noted that the spike deconvolution was suboptimal for highly noisy traces. We used the skewness of the trace as a proxy for high signal-to-noise ratio, as a trace with strong relative noise will have a distribution of $\Delta F/F_0$ close to Gaussian and therefore a skewness close to 0. We selected neurons with a skewness equal to or above 1.5 for most of the analyses. We checked the robustness of our results and found that evoked activity was much larger than spontaneous activity in SRGAP2C mice relatively to WT mice for the entire range of skewness thresholds considered (Extended Data Fig. 8d).

Modelling neural responses

We implemented a recurrent circuit model with a population of excitatory cells and a population of inhibitory cells representing neurons in layer 2/3 using the following dynamical equations (Supplementary Information):

$$\tau \frac{de}{dt} = -e + [W_{ee}e - \xi W_{ei}i + \xi \omega_{eh}h + b_e \mathbf{1}]_{\downarrow}^2$$

$$\tau \frac{di}{dt} = -i + [W_{ie}e - W_{ii}i + \omega_{ih}h + b_i \mathbf{1}]_{\downarrow}^2$$

Here, the vectors \mathbf{e} and \mathbf{i} correspond to the neural activity of excitatory and inhibitory neurons, respectively, while the vector \mathbf{h} represents the activity of input neurons from layer 4; $[x]_{\downarrow}^2$ represents a rectified quadratic function applied to the scalar x ; $W_{\alpha\beta}$ is the matrix of recurrent connections from population β to population α with $\alpha, \beta \in \{e, i\}$; the scalars $\omega_{\alpha h}$ represent the strength of feedforward connections from layer 4 to population α ; τ is the membrane time constant; and ξ is the factor giving the increase in connection strengths in the SRGAP2C (abbreviated to 2C in equations) mouse ($\xi = 1.8$ in SRGAP2C mice, $\xi = 1.0$ in WT mice). The vector $\mathbf{1}$ is the vector whose elements are all 1, and the scalars b_e and b_i are the strengths of background (stimulus-independent) inputs. The elements of the matrices $W_{\alpha\beta}$ are randomly drawn and independently and identically distributed, with mean $\langle W_{\alpha\beta} \rangle = \omega_{\alpha\beta}/n_{\beta}$ and $\text{Var}[W_{\alpha\beta}] = \sigma_{\alpha\beta}^2/n_{\beta}$, where n_{β} is the number of presynaptic connections from population β . The scalars $\omega_{\alpha h}$ represent the feedforward connection strengths from the layer 4 excitatory neurons to the layer 2/3 population α . The elements of the vector \mathbf{h} are randomly drawn with mean $\langle h_j \rangle = \mu_h$ and $\text{Var}[h_j] = \zeta_h^2$. The various parameters are fit as described below. We selected a quadratic input/output function because power laws phenomenologically describe neurons in mouse V1 (refs. ³³⁻³⁵) and because our previous work has demonstrated that neurons with such input/output functions capture many properties of cortical circuits^{36,37}. Note that a rectified quadratic power law was able to capture the distribution of firing rates across different

Article

conditions, although this would not have been possible with a linear transfer function, which could only generate Gaussian distributions (see the discussion in the Supplementary Information).

We optimized the parameters $\omega_{\alpha\beta}$, $\sigma_{\alpha\beta}$, ω_{ah} , μ_h (stimulus = spontaneous), μ_h (stimulus = evoked), c_h and b_α following a two-step procedure. First, similar to Keller et al.³⁸, we optimized the parameters other than $\sigma_{\alpha\beta}$ and c_h in a two-unit population model described by the following equations:

$$\tau \frac{d\mu_e}{dt} = -\mu_e + [\omega_{ee}\mu_e - \xi\omega_{ei}\mu_i + \xi\omega_{eh}\mu_h + b_e]_+^2$$

$$\tau \frac{d\mu_i}{dt} = -\mu_i + [\omega_{ie}\mu_e - \omega_{ii}\mu_i + \omega_{ih}\mu_h + b_i]_+^2$$

We independently generated $N_p = 1,000,000$ different values of $\omega_{\alpha\beta}$ and of ω_{ah} from gamma distributions of mean and standard deviation equal to 2. Similarly, we generated N_p different values of b_α from a Gaussian distribution of mean 0 and standard deviation 1. Then, we generated μ_h (spontaneous) and μ_h (evoked) from two gamma distributions of mean 0.5 and 1 for spontaneous and evoked activity, respectively. If for a set of parameters μ_h (s = spontaneous) $>$ μ_h (s = evoked), we switched the two. We fixed $\tau = 10$ ms and evolved the dynamical equations using an Euler scheme. Finally, when the system converged to a stable fixed point, we compared the rates to the data by minimizing

$$\text{Error} = \sum_{\xi \in \{1,1.8\}} \sum_{s \in \{\text{spontaneous, evoked}\}} [\mu_e^{\text{model}}(\xi, s) - \mu_e^{\text{data}}(\xi, s)]^2 + \lambda_1 \sum_{\alpha\gamma} \omega_{\alpha\gamma}^2 + \lambda_2 \sum_{\alpha\gamma} [-\log \omega_{\alpha\gamma}]_+$$

where y represent either one of the two layer 2/3 populations e and i or the layer 4 input h and with $\lambda_1 = 0.1$ and $\lambda_2 = 5 \times 10^{-5}$, which ensured that the weights were neither too close to 0 nor too large³⁸. We selected the 20 parameter sets with the minimum value of Error after removing solutions not satisfying the following equation:

$$y := \frac{\mu_e^{\text{model}}(\xi = 2C, s = \text{evoked})}{\mu_e^{\text{model}}(\xi = 2C, s = \text{spontaneous})} / \frac{\mu_e^{\text{model}}(\xi = \text{WT}, s = \text{evoked})}{\mu_e^{\text{model}}(\xi = \text{WT}, s = \text{spontaneous})} > 1$$

In these top 20 solutions, the excitatory-to-excitatory connections were typically weak, and they were the weakest of the recurrent connections (16 out of 20 solutions). Conversely, inhibitory-to-inhibitory connections were typically the strongest of the recurrent connections (14 out of the 20 solutions). Although not all solutions satisfy $y > 1$, we found that the more closely the generated parameter sets match the activity of WT mice, the higher the proportion of solutions satisfying $y > 1$. To demonstrate this, we generated 10,000,000 parameter sets as before and discarded all unstable solutions (44.6%). Among the stable solutions, we considered the solutions with error on the WT activity below a given threshold and varied the threshold (so that the lower the threshold, the fewer the number of solutions considered). We observed that the lower the error threshold (the more closely the solutions matched WT activity), the more solutions satisfied $y > 1$ (Extended Data Fig. 8h). In particular, when considering the 2,000 solutions that best fit the WT data, 78.8% satisfied $y > 1$. In the second step, we tested 15 different values of noise in the recurrent connection strengths $\sigma_{\alpha\beta} \in [0, 7\omega_{\alpha\beta}]$ (including the factor ξ when appropriate) and 11 different values of noise in the inputs $c_h \in [0, 0.035]$ with a grid search using, for the other parameters, the 20 top solutions generated from the first step. Among the resulting solutions, we selected the one that was most robust in reproducing the data in terms of variation of $\sigma_{\alpha\beta}$ and c_h , as follows. We selected the one for which (1) the Wasserstein

distance between the probability distribution of responses (evoked – spontaneous activity) in the model and in the data (summed over WT and SRGAP2C mice) was smaller than 1.5 and (2) the difference between responses (evoked – spontaneous activity) was on average the closest to the data for the largest range of $\sigma_{\alpha\beta}$ and c_h : defining $\Delta\mu = \mu_e$ (stimulus = spontaneous) – μ_e (stimulus = evoked), we chose the solution that satisfied (1) and satisfied $(\Delta\mu_{2C}^{\text{model}} - \Delta\mu_{WT}^{\text{model}}) - (\Delta\mu_{2C}^{\text{data}} - \Delta\mu_{WT}^{\text{data}}) / \text{s.d.}(\{\Delta\mu_{2C}^{\text{data}}, \Delta\mu_{WT}^{\text{data}}\}) < 0.5$

for the largest number of combinations of $\sigma_{\alpha\beta}$ and c_h . We generated the values of $W_{\alpha\beta}$ by sampling over gamma distributions and the values of \mathbf{h} by sampling over Gaussian distributions. Finally, for the chosen solution, we selected the values of $\sigma_{\alpha\beta}$ and c_h that maximized the following function:

$$\left(1 - \frac{N_{2C} + N_{WT}}{2}\right) + \lambda_3 \left(\frac{N_{2C} - N_{WT}}{2}\right)$$

with $\lambda_3 = 10$, where N_{WT} and N_{2C} are the fraction of neurons increasing their responses from spontaneous to evoked activity in the WT mice or SRGAP2C mice, respectively. This ensured that the fraction of neurons increasing their responses, summed over SRGAP2C and WT mice, was as small as possible (because it was difficult in the model to have as many neurons decreasing their response as in the data, so this pushed the model in the direction of having more neurons decreasing their response). It also ensured that the difference between the SRGAP2C and WT mice in the number of neurons increasing their responses was as large as possible, with the second weighted ten times more strongly than the first. For a fixed set of parameters these properties were robust across different initializations of the random weights (see below).

The selected model had the following parameters (approximately): $n_y = 1,000$, $\omega_{ee} = 0.34$, $\omega_{ei} = 0.76$, $\omega_{ie} = 0.39$, $\omega_{ii} = 4.27$, $\sigma_{\alpha\beta} = 0.045 \times \omega_{\alpha\beta}$ for the recurrent connections; $\omega_{eh} = 0.69$, $\omega_{ih} = 1.97$; μ_h (s = spontaneous) = 0.50, μ_h (s = evoked) = 0.81, $c_h = 0.37$; $b_e = 0.15$, and $b_i = -0.34$. We ran 100 simulations with different random seeds and N_{2C} was larger than N_{WT} in all of them. The network would reproduce qualitatively the effects described in the main text for a reasonable range of parameters, for example, when varying $\sigma_{\alpha\beta}$ and c_h while fixing all other parameters. Simulations were performed using Python, Matplotlib, NumPy, SciPy and sklearn.

Texture-discrimination task

Surgeries. Adult mice were anaesthetized using isoflurane and injected with meloxicam, after which the dorsal skull was exposed and cleaned with a scalpel. A custom-designed steel head plate (Wilke Enginuity) was subsequently secured onto the skull using Metabond (Parkell).

Behavioural setup. The behavioural apparatus was contained within a black box (Foremost) with a light-blocking door. A stepper motor (Pololu) rotated custom-designed textures in position, after which they were advanced into the final stimulus position within approximately 1 cm of the right whisker pad of the mouse using a linear actuator (Actuonix L12-30-50-6-R). Textures were laser cut from acrylic sheets to a dimension of 16 × 33 mm. Vertical grooves of approximately 500 μ m deep and 350 μ m wide were laser cut into the acrylic textures at a spacing of 200 or 2,000 μ m apart. These were identified as R200 and R2000, respectively. Rewards (approximately 5 μ l of water) were delivered by opening a solenoid valve (The Lee, LFAA1209512H) that allowed water to flow from a reservoir to the lick port, which was made of a stainless-steel tube (McMaster). Two lick ports were positioned in front and slightly to the left and right of the mouth of the mouse, and licking was registered using capacitive touch sensors (Sparkfun MPR121). Between trials, a white light (LE LED 1800016-WW-US) was activated to prevent mice from fully dark-adapting. This prevented mice from using visual cues in performing the task. A computer fan

(Cooler Master 80 mm Silent Fan) blew air over the texture away from the mouse, which prevented the mouse from picking up olfactory cues. In addition, the textures were regularly cleaned with 70% ethanol. We never observed mice exploiting auditory or vibrational cues from the motors; therefore, no masking noises were necessary.

All aspects of the task were controlled by an Arduino Uno. A desktop PC chose the stimulus and correct response and logged all events read from the Arduino to disk using custom Python code. The training parameters for each mouse were stored in a custom-written Django database and updated manually or semi-manually by the experimenters depending on the progress of each mouse.

Mouse training and testing. Experimenters were blind to the genotype of mice during every step of training and testing. Mice were denied water access in the home cage and learned to receive their water during the behavioural training. For each mouse, we closely monitored water intake, weight and general health to ensure that they did not suffer from dehydration. Ad libitum water was provided as necessary to prevent adverse effects on health. Mouse training was performed according to the following pipeline (Fig. 4b). (1) Handling and free licking. During this stage, mice were handled to become familiar with the experimenters. By placing mice in the set up without head-fixing and allowing them to drink freely from the water pipes, they also became familiar with the behavioural set up. This stage required on average four sessions. (2) Head-fixed lick training. Mice were head-fixed directly in front of a single lick pipe and received a water reward for every lick. Next, mice were presented with two lick pipes on the left and right side of their mouth and learned to lick alternately from each of them. This lick training started with mice alternating after every ten licks and was gradually decreased to a single lick on each side. This stage required on average four sessions. (3) Pre-training. Here, mice were presented with the complete trial structure for the first time (that is, textures were presented and mice were only rewarded for correct responses). Incorrect responses were punished with a timeout. Presentation of the same texture was repeated until mice correctly responded, after which the other texture was presented. Thus, mice could perform at 100% by alternating responses from trial to trial. The timeout was initially 2 s and gradually increased to 9 s as mouse performance increased. This stage required between 10 and 15 sessions. (4) Training. Each session began with 45 trials of pre-training (as in step 3) to verify that mice were able to lick both lick ports. After these initial pre-training trials, presentation of textures was randomized. The software continuously monitored mouse performance for biases, whereby mice stopped alternating between lick pipes and focused on one lick pipe only. When a strong bias was detected, presentation of the textures stopped being random and was presented to counteract the bias: if mice responded $\geq 20\%$ more on one side than the other, the software would deliver only trials opposite to the biased side. If mice showed a significant perseverative bias ($P < 0.05$, analysis of variance), the software would deliver alternating trials. For analysis, non-randomized trials were excluded and only randomized trials were used to assess performance.

Finally, to assess that mice relied on their whiskers to discriminate between textures, whiskers facing the texture side were fully trimmed. If performance did not fall to chance ($< 60\%$ correct), mice were excluded from analysis. One mouse was excluded on the basis of this criterion.

Statistics and reproducibility

Statistical analysis was performed using Prism v.6, v.8 and v.9 (Graphpad Software). Normality was checked using Kolmogorov–Smirnov test. A nonparametric test (Kruskal–Wallis with post hoc Dunn’s multiple comparison test or Mann–Whitney U -test) was used when distribution deviated significantly from normality. A test was considered significant when $P < 0.05$. For RABV tracing, ten WT littermate controls and seven SRGAP2C mice were obtained from a minimum of four independent litters. For in vivo spine analysis, data were obtained from at least six

animals from a minimum of three independent litters. For two-photon microscopy experiments, four WT littermate controls and three SRGAP2C mice were obtained from two independent litters. For the texture-discrimination task, 20 WT littermate controls and 18 SRGAP2C mice were tested across two separate cohorts from a minimum of four independent litters. Significance was tested using a chi-squared test. Independent data points shown denote data from individual animals. Each experiment was repeated at least three times with similar results.

Reporting summary

Further information on research design is available in the Nature Research Reporting Summary linked to this paper.

Data availability

The reagents, mouse line and datasets generated and/or analysed during the current study are available from the corresponding author upon request.

Code availability

Custom-written Matlab and Python code is available upon request from the corresponding author.

26. Courchet, J. et al. Terminal axon branching is regulated by the LKB1–NUAK1 kinase pathway via presynaptic mitochondrial capture. *Cell* **153**, 1510–1525 (2013).
27. Hand, R. & Polleux, F. Neurogenin2 regulates the initial axon guidance of cortical pyramidal neurons projecting medially to the corpus callosum. *Neural Dev.* **6**, 30 (2011).
28. Paxinos, G. & Franklin, K. B. J. *The Mouse Brain in Stereotaxic Coordinates* (Academic, 2001).
29. Ma, Y. et al. Wide-field optical mapping of neural activity and brain haemodynamics: considerations and novel approaches. *Philos. Trans. R. Soc. B Biol. Sci.* **371**, 20150360 (2016).
30. Pnevmatikakis, E. A. & Giovannucci, A. NoRMCorre: an online algorithm for piecewise rigid motion correction of calcium imaging data. *J. Neurosci. Methods* **291**, 83–94 (2017).
31. Peters, A. J., Chen, S. X. & Komiyama, T. Emergence of reproducible spatiotemporal activity during motor learning. *Nature* **510**, 263–267 (2014).
32. Deneux, T. et al. Accurate spike estimation from noisy calcium signals for ultrafast three-dimensional imaging of large neuronal populations in vivo. *Nat. Commun.* **7**, 12190 (2016).
33. Hansel, D. & van Vreeswijk, C. How noise contributes to contrast invariance of orientation tuning in cat visual cortex. *J. Neurosci.* **22**, 5118–5128 (2002).
34. Miller, K. D. & Troyer, T. W. Neural noise can explain expansive, power-law nonlinearities in neural response functions. *J. Neurophysiol.* **87**, 653–659 (2002).
35. Priebe, N. J. & Ferster, D. Inhibition, spike threshold, and stimulus selectivity in primary visual cortex. *Neuron* **57**, 482–497 (2008).
36. Rubin, D. B., Van Hooser, S. D. & Miller, K. D. The stabilized supralinear network: a unifying circuit motif underlying multi-input integration in sensory cortex. *Neuron* **85**, 402–417 (2015).
37. Hennequin, G., Ahmadian, Y., Rubin, D. B., Lengyel, M. & Miller, K. D. The dynamical regime of sensory cortex: stable dynamics around a single stimulus-tuned attractor account for patterns of noise variability. *Neuron* **98**, 846–860.e5 (2018).
38. Keller, A. J. et al. A disinhibitory circuit for contextual modulation in primary visual cortex. *Neuron* **108**, 1181–1193.e8 (2020).

Acknowledgements The transgenic inducible knock-in mouse model described here was developed in collaboration with genOway (Lyon, France). We thank T. Reardon and S. Fageiry for providing RABV; M. Hirabayashi and Q. Liu for technical help; D. Peterka and the staff at the Zuckerman Institute’s Cellular Imaging platform for instrument use and technical advice; and members of the Polleux laboratory and P. Vanderhaeghen for valuable discussions and input. This work was supported by NIH R01 (RO1NS067557) (to F.P.); an award from the Roger De Spoelberch Foundation (to F.P.); an award from the Nomis Foundation (to F.P.); the Netherlands Organization for Scientific Research (NWO Rubicon 825.14.017) (to E.R.E.S.); the European Molecular Biology Organization (EMBO Long-Term Fellowship ALTF 1055-2014) (to E.R.E.S.); NIH K99 (NS109323) (to E.R.E.S.); NSF GRFP (to J.M.P.); NIH R01 (NS094659) and NIH R01 (NS069679) (to R.M.B.); NIH U19 (U19NS107613) (to M.D., M.M.M.-M. and K.D.M.); a NSF NeuroNex Award (DBI-1707398) (to K.D.M. and M.D.); The Gatsby Charitable Foundation (GAT3708) (to K.D.M. and M.D.); the Simons Collaboration on the Global Brain (543017) (to K.D.M. and M.D.); and R01 NS063226, RF1 MH114276, U11 NS108213 and U19NS104649 (to E.M.C.H.).

Author contributions E.R.E.S. and F.P. conceived the experiments. E.R.E.S. carried out the RABV tracing and synaptic analysis. E.R.E.S. and A.L. performed the spine quantifications, and E.R.E.S. and H.T.Z. performed the two-photon imaging experiments. C.C.R., J.M.P. and R.M.B. developed the texture-discrimination behaviour experiments, and E.R.E.S., J.M.P. and J.B.D. performed these experiments. M.D., M.M.M.-M. and K.D.M. performed the data analysis and computational modelling shown in Extended Data Figs. 8 and 9. E.R.E.S., H.T.Z. and J.M.P. analysed the data. R.M.B. advised on the behavioural experimental design, and E.M.C.H. and R.M.B. advised on the two-photon data analysis. E.R.E.S. and F.P. wrote the manuscript.

Article

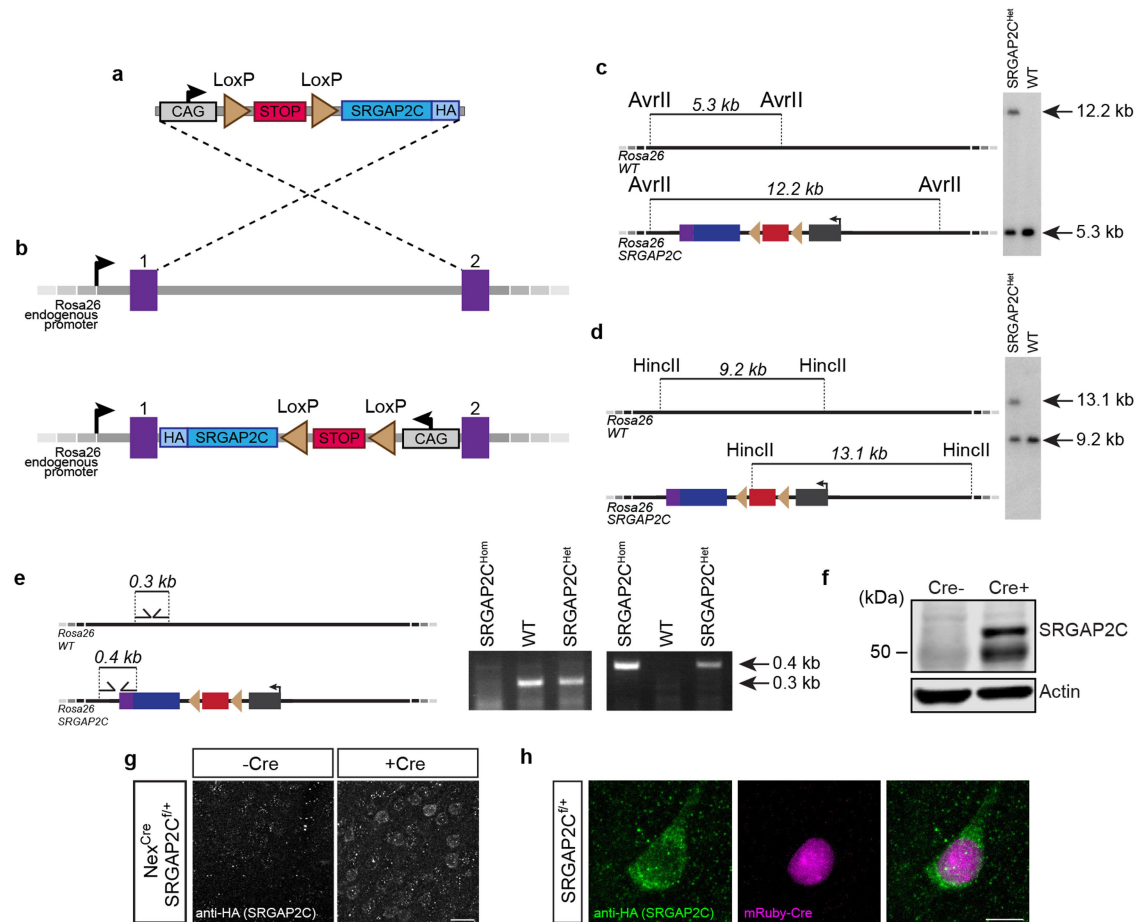
Competing interests The authors declare no competing interests.

Additional information

Supplementary information The online version contains supplementary material available at <https://doi.org/10.1038/s41586-021-04039-4>.

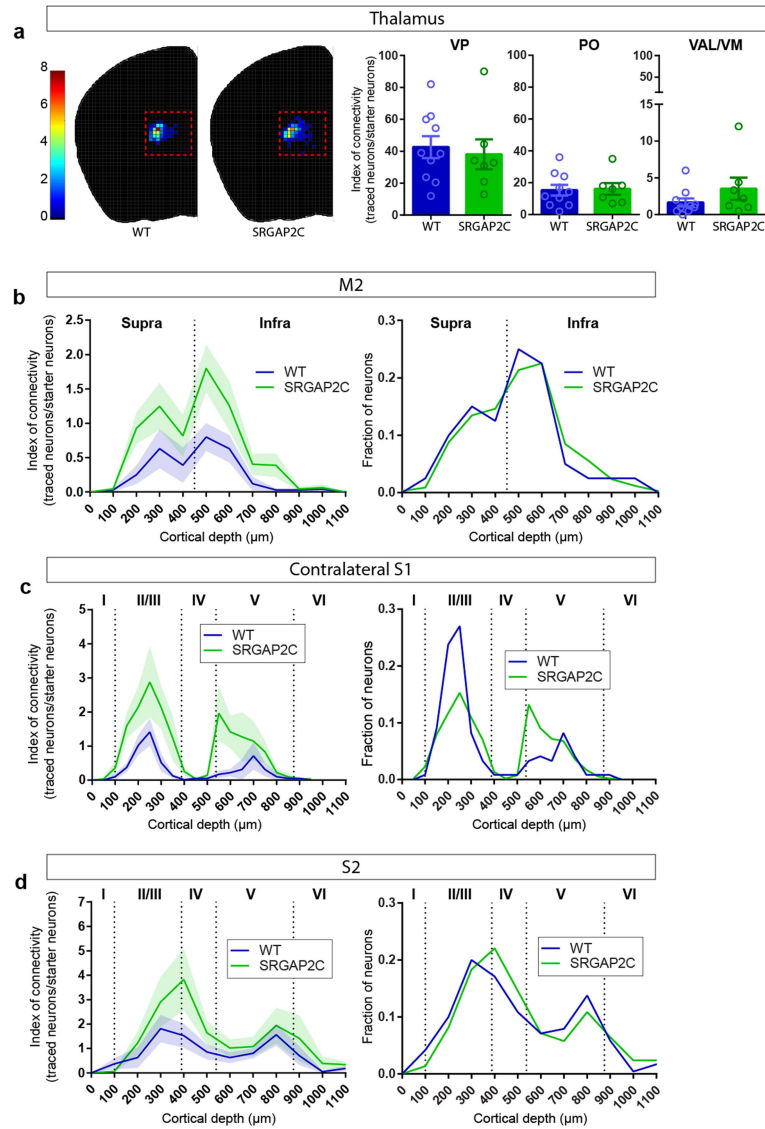
Correspondence and requests for materials should be addressed to Franck Polleux.
Peer review information *Nature* thanks Tatiana Engel and the other, anonymous, reviewer(s) for their contribution to the peer review of this work.

Reprints and permissions information is available at <http://www.nature.com/reprints>.



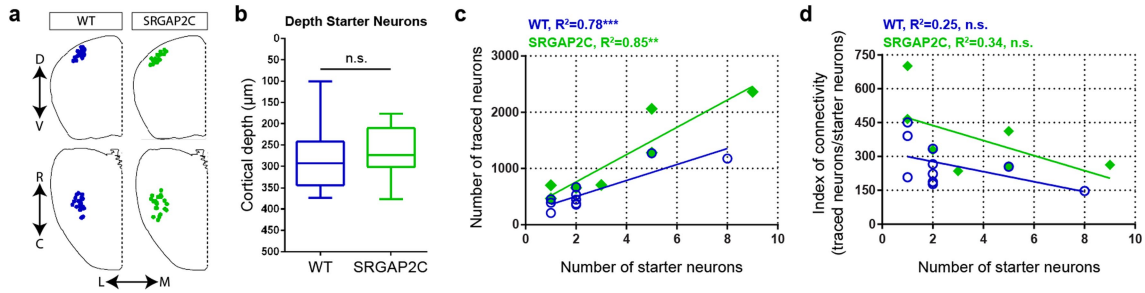
Extended Data Fig. 1 | Generation of an inducible, humanized SRGAP2C transgenic mouse line. (a–b) Design strategy for generating SRGAP2C conditional knock in mice. 3x HA tagged *SRGAP2C* was inserted into a *Rosa26* targeting vector (a), which contains a CAG promoter, a floxed STOP-Neomycin cassette, and *Rosa26* homology arms. Image not to scale. Using homologous recombination, the targeting vector was inserted between exon1 and 2 of the *Rosa26* locus (b). (c–d) Verification of SRGAP2C targeting in mouse embryonic stem cells using Southern blot analysis with probes that distinguish the targeted allele (12.2 kb in (c), 13.1 kb in (d)) from the wild-type allele (5.3 kb in (c), 9.2 kb in (d)). (e) Mice were genotyped by genomic PCR using the forward and reverse primers indicated that distinguish the WT *Rosa26* allele or the

SRGAP2C allele. (f) Western blot probed with anti-HA antibody of adult (P30) cortex isolated from SRGAP2C heterozygous conditional knock-in mice crossed with heterozygous *Nex^{Cre/+}* mice (Cre+) or wild-type littermate (Cre-). The presence of Cre induces SRGAP2C-HA expression. Without Cre, no SRGAP2C was detected. Anti-Actin antibody was used as loading control. (g) Immunohistochemistry for HA on cortical brain sections from adult SRGAP2C heterozygous conditional knock-in mice crossed with heterozygous *Nex^{Cre/+}* mice (Cre+) or wild-type littermate control (Cre-). Scale bar, 25 μ m. (h) Same as g, on sections from SRGAP2C heterozygous conditional knock-in mice in which mRuby-Cre was sparsely expressed using *in utero* cortical electroporation. Scale bar, 10 μ m.



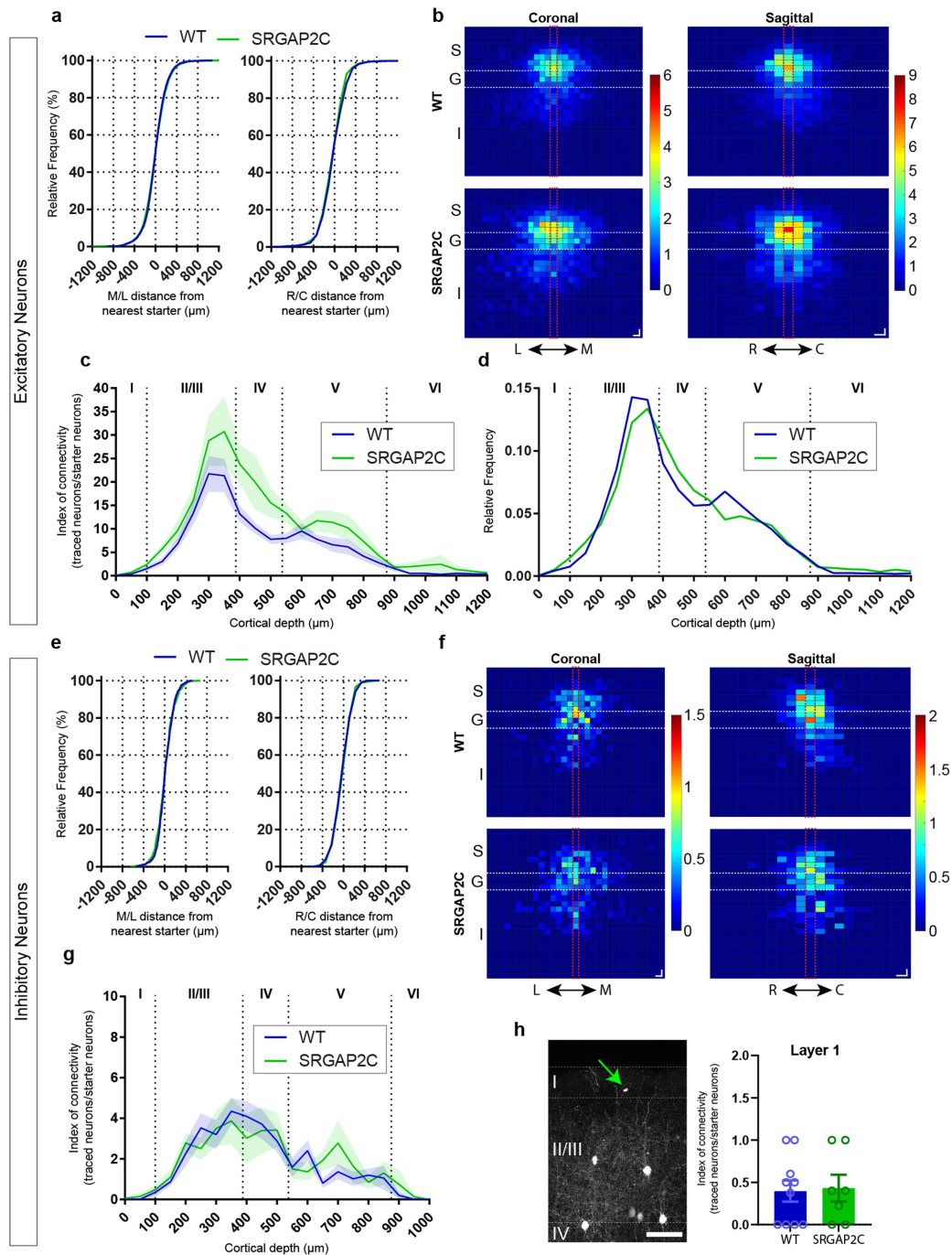
Extended Data Fig. 3 | Distribution of RABV traced neurons. (a) Index of connectivity (IOC, number of traced neurons / number of starter neurons) for traced neurons in the thalamus. No difference was observed between WT and SRGAP2C mice (two-sided Mann-Whitney test). Left: distribution of traced neurons in WT and SRGAP2C, colors indicate IOC. Right: IOC for

Ventralanteriorlateral/medial (VAL/VM), Ventralposterior (VP), and Posterior (PO) thalamic subnuclei. Bar graphs plotted as mean \pm s.e.m. Open circles in bar graphs indicate individual mice ($n = 10$ for WT and $n = 7$ for SRGAP2C mice). **(b–d)** Distribution of traced neurons as a function of their cortical depth. Left: IOC, right: fraction. Shaded area indicates s.e.m.



Extended Data Fig. 4 | Connectivity changes are not caused by differences in cortical depth or number of starter neurons. (a) Anatomical location of starter neurons. (b) Cortical depth of starter neurons measured as distance from pial surface is not different between WT and SRGAP2C mice, two-sided Mann-Whitney test. Data shown as box-and-whisker plots. Center line indicates median, box edges represent first and third quartiles, and whiskers represent minimum and maximum values ($n = 26$ starter neurons from 10 WT mice and

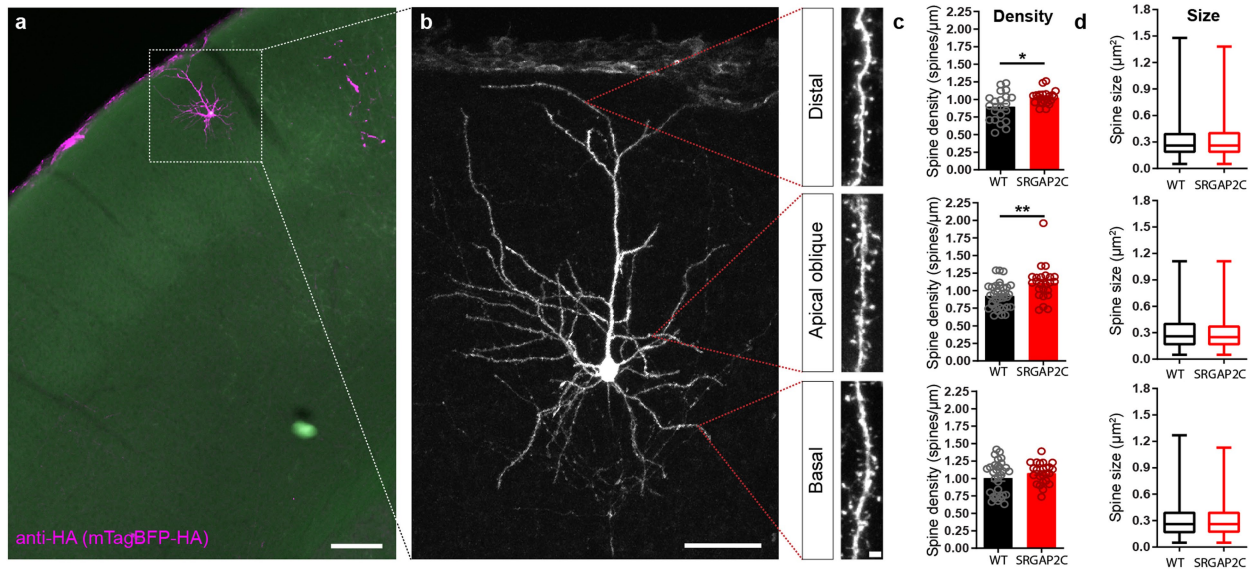
$n = 26$ starter neurons from 7 SRGAP2C mice). (c) Correlation between number of RABV infected starter neurons and RABV traced neurons (Pearson's correlation coefficient $r = 0.88$, $P = 7 \times 10^{-4}$ for WT, and $r = 0.92$, $P = 3.2 \times 10^{-3}$ for SRGAP2C). (d) No correlation was observed between IOC and number of RABV infected starter neurons per brain (Pearson's correlation coefficient $r = -0.5$, $P = 0.14$ for WT, and $r = -0.58$, $P = 0.17$ for SRGAP2C).



Extended Data Fig. 5 | Distribution of RABV traced neurons locally in S1.

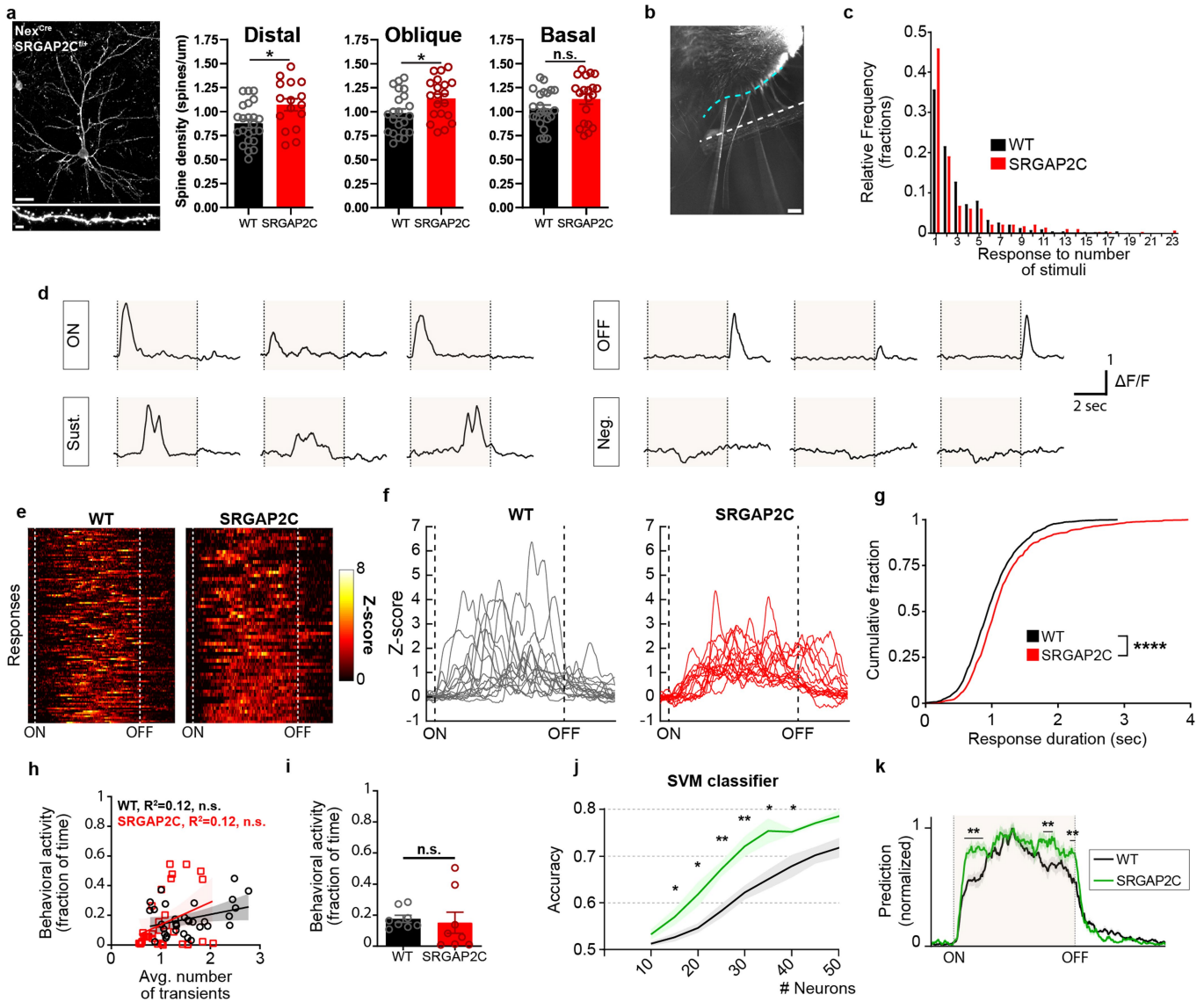
(a) Distance between RABV traced excitatory neurons in S1 and their closest starter neuron along the medial/lateral (M/L) or rostral/caudal (R/C) plane. No difference was observed between WT and SRGAP2C mice (Kolmogorov-Smirnov test). Data shown as relative frequency distribution. (b) Density plots showing distribution of traced excitatory neurons relative to their closest starter neuron for coronal (left, L and M indicate lateral and medial orientation, respectively) and sagittal view (right, R and C indicate rostral and caudal orientation, respectively). Center bins aligned with relative position of starter neuron are indicated by red dashed lines. S, supragranular, G, granular, I, infragranular layers. For coronal, bin size = 50x50 μm . For sagittal, bin size = 50x100 μm . Colors in density plots indicate IOC. (c) Cortical layer distribution of RABV traced excitatory neurons in S1 shown as Index of

connectivity (IOC, number of traced neurons / number of starter neurons). Shaded are indicates s.e.m. (d) Fraction of RABV traced neurons across cortical layers in S1. Dashed lines indicate borders between layers. Roman numbers identify cortical layers. (e) Same as (a), for inhibitory neurons. For analysis of interneurons, Parvalbumin-positive and Somatostatin-positive were grouped together. (f) Same as (b), for inhibitory neurons. Shaded are indicates s.e.m. (g) Same as (c), for inhibitory neurons. Shaded are indicates s.e.m. (h) RABV traced neurons in layer 1. Left: Coronal section showing location of a layer 1 traced neuron (green arrow) in the barrel field of the primary sensory cortex (S1). Right: IOC for layer 1 traced neurons. No difference was observed between WT and SRGAP2C mice (Mann-Whitney test). Scale bar, 100 μm . Bar graphs plotted as mean \pm s.e.m. Open circles in bar graphs indicate individual mice ($n = 10$ for WT and $n = 7$ for SRGAP2C mice).



Extended Data Fig. 6 | SRGAP2C expression selectively increases synaptic density on apical dendrites. (a) Coronal section stained for HA showing sparse labeling of a layer 2/3 cortical pyramidal neuron in the barrel field of the primary somatosensory cortex. Scale bar, 150 μm . (b) Higher magnification of neuron in (a). Red dotted lines indicate approximate location where spine density and size were quantified for distal, apical oblique, and basal dendritic compartments. Panels on right show high magnification images of dendritic segments on which spines can clearly be identified. Left panel scale bar, 50 μm . Right panel scale bar, 2 μm . (c) Spine density is increased for distal, and apical but not basal dendritic segments. ($P = 1.92 \times 10^{-2}$ for distal, $P = 1.5 \times 10^{-3}$ for apical oblique, $P = 0.3$ for basal; distal: $n = 21$ segments for WT and SRGAP2C,

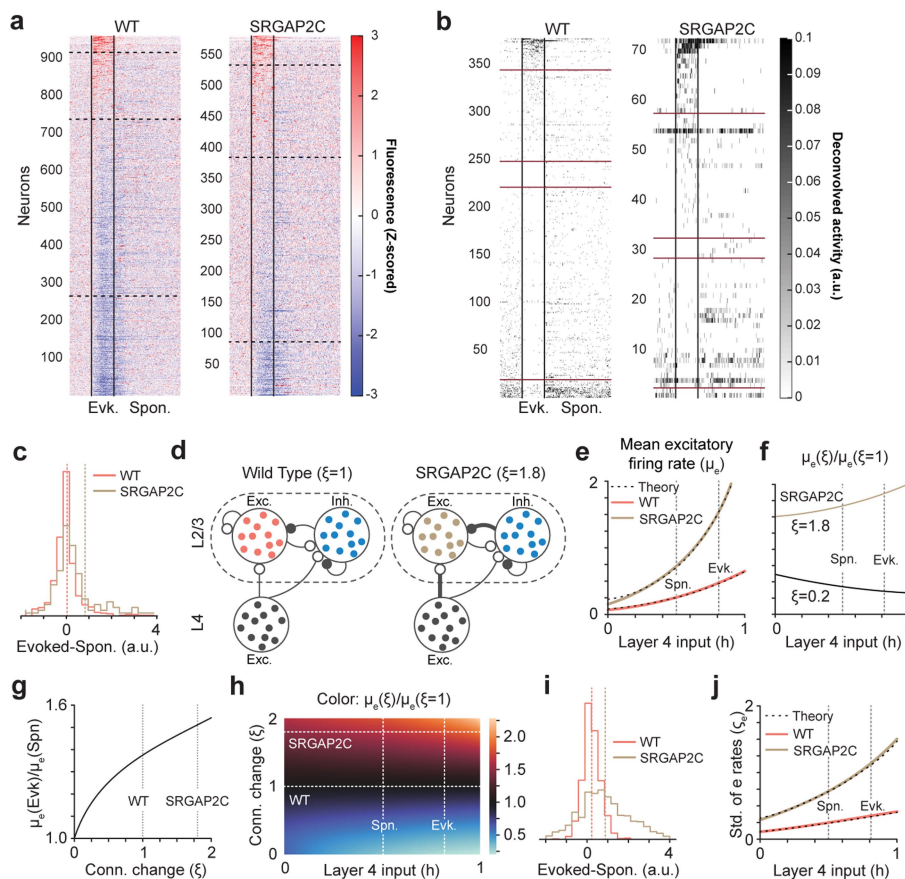
apical oblique: $n = 33$ segments for WT and $n = 24$ segments for SRGAP2C, basal: $n = 32$ segments for WT and $n = 24$ segments for SRGAP2C). Bar graph plotted as mean \pm s.e.m. * $P < 0.05$, ** $P < 0.01$, two-sided Mann-Whitney test. (d) Spine size is not significantly changed in adult SRGAP2C expressing layer 2/3 cortical pyramidal neurons. Data shown as box-and-whisker plots. Center line indicates median, box edges represent first and third quartiles, and whiskers represent minimum and maximum values (distal: $n = 1273$ spines for WT and $n = 1083$ spines for SRGAP2C, apical oblique: $n = 2401$ spines for WT and $n = 1650$ spines for SRGAP2C, basal: $n = 2286$ spines for WT and $n = 1448$ spines for SRGAP2C).



Extended Data Fig. 7 | Neuronal responses following whisker stimulation.

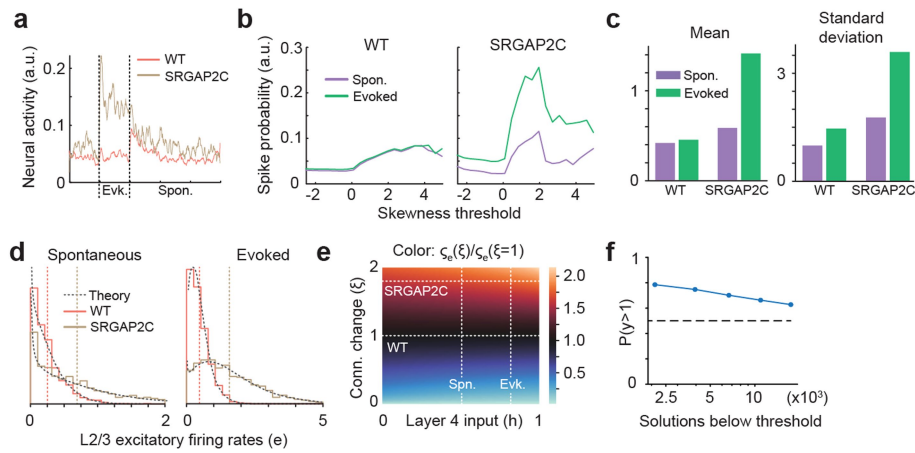
(a) Left: Coronal section stained for HA showing sparse labeling of a layer 2/3 cortical pyramidal neuron in the barrel field of the primary somatosensory cortex with high magnification (bottom) of dendritic segment in which spines can clearly be identified. Scale bar top, 25 μm . Scale bar bottom, 2 μm . Right: Spine density quantification in SRGAP2C heterozygous conditional knock-in mice crossed with heterozygous Nex^{Cre/+} mice. Spine density is increased for distal and apical but not basal dendritic segments ($P = 1.34 \times 10^{-2}$ for distal, $P = 2.47 \times 10^{-2}$ for apical oblique, $P = 0.117$ for basal; distal: $n = 23$ segments for WT and $n = 16$ for SRGAP2C, apical oblique: $n = 22$ segments for WT and $n = 20$ segments for SRGAP2C, basal: $n = 23$ segments for WT and $n = 20$ segments for SRGAP2C). Bar graph plotted as mean \pm s.e.m. * $P < 0.05$, two-sided Mann-Whitney test. (b) Top-down view of placement of stimulating rod (white dashed line, 2mm away from the whisker pad) next to right whisker pad (cyan dashed line). Scale bar, 1mm. (c) Frequency distribution of response fraction for neurons responding to either onset, sustained phase, or offset of the stimulus. (d) Single-trial example responses. Shaded area indicates whisker

stimulation. (e) Ten percent of single trial Sustained responses with longest sustained activity converted to Z-scores and sorted by duration of response. ON and OFF dashed lines indicate stimulus onset and offset, respectively (f) Bottom 15 responses shown in (e). (g) Cumulative probability distribution of Sustained response durations (time that Z-score was greater than 1). $P < 1 \times 10^{-4}$, Kolmogorov-Smirnov test. (h) Correlation between behavioral activity and average number of transients ($n = 32$ runs for 8 FOVs from 4 WT mice and $n = 32$ runs for 8 FOVs from 3 SRGAP2C mice). (i) Fraction of time during which behavioral activity was observed ($n = 8$ FOVs from 4 WT and $n = 8$ FOVs from 3 SRGAP2C mice). Bar graph plotted as mean \pm s.e.m., two-sided Mann-Whitney test. (j) Support vector machine (SVM) accuracy in classifying presence or absence of whisker stimulus. Shaded area indicates s.e.m. (k) Normalized SVM prediction accuracy across time from stimulus ON to stimulus OFF for 25 neurons per field of view. Shaded area indicates stimulus time. Multiple t-test with multiple comparison correction using false-discovery rate Benjamini-Hochberg method ($q < 0.05$), * $P < 0.05$, ** $P < 0.01$.



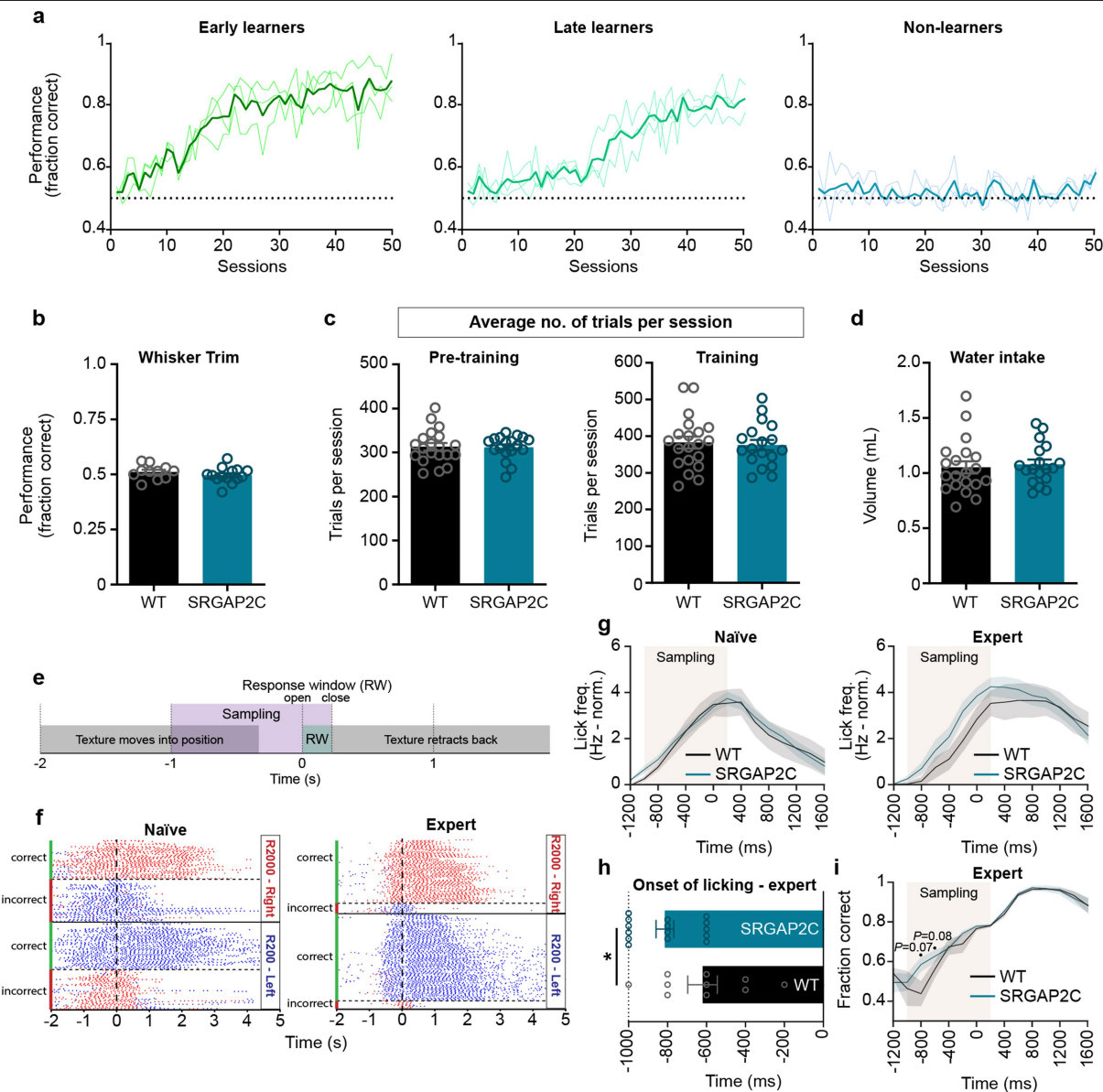
Extended Data Fig. 8 | Computational modelling of increased layer 4 to layer 2/3 connectivity explains observed SRGAP2C neuronal response properties. (a) Stimulus-triggered average fluorescence for all neurons recorded in WT and SRGAP2C mice. Fluorescence has been Z-scored and average activity during the 5 s prior to the stimuli have been subtracted. Horizontal dashed lines correspond to the separation between neurons that significantly increase (top) or decrease (bottom) their activity during evoked activity. Vertical solid lines correspond to stimulus onset and offset. Layer 2/3 PNs have been sorted according to the robustness of their signed response to the stimulus. (b) Stimulus-triggered average neural activity (after deconvolving fluorescence) for neurons with high signal-to-noise ratio. Horizontal red lines correspond to the separation between neurons that significantly increase (top) or decrease (bottom) their activity during evoked activity. Neurons between the middle horizontal red lines had an equal average response during spontaneous and evoked activity (typically 0). Neurons have been sorted according to the strength of their signed response to the stimulus. (c) The normalized distributions of firing rate differences between whisker stimulation and spontaneous activity. Dashed vertical lines indicate means of the distributions. (d) The model considers a population of excitatory neurons in layer 4 (gray) projecting to populations of inhibitory (blue) and excitatory (red, brown) neurons in cortical layer 2/3 of barrel cortex. The strength of the projections targeting layer 2/3 PNs and coming from layer 4 excitatory and layer 2/3 inhibitory neurons is assumed to be larger in SRGAP2C mice than WT

mice by a factor ξ , as indicated. All neurons are modelled with a quadratic I/O transfer function. (e) The mean rate of simulated excitatory units (μ_e) in SRGAP2C mice (brown) are higher and increase at a higher rate than those in WT mice (red) as a function of the mean excitatory input h from layer 4. This is particularly true for the rates at the input levels we model as spontaneous and evoked activity (left and right gray vertical dashed lines, respectively). A mathematical approximation (black dashed lines; Supplementary Material) agrees to an excellent degree with the simulations. (f) The model ratio of mean excitatory rates between SRGAP2C mice ($\xi = 1.8$, top black curve) or mice with a hypothetical decrease in connection strength ($\xi = 0.2$, bottom black curve) and WT mice. (g) The model ratio between the mean excitatory rate during evoked vs. spontaneous activity monotonically increases with the change in connectivity relative to WT mice. (h) The model ratio of mean excitatory rates between mice with an arbitrary change in connection strength and WT mice. (i) The normalized distributions of firing rate differences between evoked and spontaneous mean input in the model. As in the experimental data (panel c), both model SRGAP2C and model WT mice contain subgroups of neurons that increase and subgroups that decrease their activity in going from spontaneous to evoked stimulation; and the fraction of neurons increasing their activity is higher in SRGAP2C mice than WT mice. (j) As for the mean rates (panel e), the variances of excitatory units in model SRGAP2C mice (brown) are higher, and increase at a higher rate as a function of the mean excitatory input from layer 4, than those in model WT mice (red).



Extended Data Fig. 9 | Modelling of layer 2/3 PN response properties in WT and SRGAP2C mice. (a) Population stimulus-triggered-average neural activity obtained by averaging over all neurons in Extended Data Figure 8b. Vertical dashed lines correspond to stimulus onset and offset. (b) Average neural activity computed during the 5s before the stimulus (Spon.) or during the 5s of stimulation (evoked; stimulus is applied at time 0) across all selected neurons and trials as a function of the skewness threshold used to select neurons. The threshold in (a) is 1.5. (c) Mean and standard deviation of the deconvolved traces in Extended Data Figure 8b during both stimulus conditions. (d) The normalized distributions of simulated excitatory rates in both SRGAP2C (brown) and WT (red) mice and during spontaneous and evoked

mean input illustrate the increase in the mean and variance discussed in the main text. The shapes of the distributions agree with their mathematical approximations (dashed black line) discussed in Supplementary Material. (e) The ratio of the standard deviation of excitatory rates between mice with an arbitrary change in connection strength and WT mice. This demonstrates that the effects are robust to the specific choice of parameters. (f) Probability of solutions with $y > 1$ as a function of the number of solutions with a fit with error of the firing rates of the wild type mouse below a certain threshold, where $y = [\mu(2c, \text{evoked})/\mu(2c, \text{spont})]/[\mu(\text{wt}, \text{evoked})/\mu(\text{wt}, \text{spont})]$ and μ corresponds to the mean firing rate of the excitatory population.



Extended Data Fig. 10 | Whisker-based texture discrimination task.

(a) Example learning curves (lighter shades) of three individual mice. Mean learning curve is shown in darker shade (b) Performance (fraction correct) after whiskers facing texture were trimmed dropped to chance level, showing that mice needed their whiskers to perform this task ($n = 11$ for WT and $n = 14$ for SRGAP2C mice). (c) Average number of trials per session for pre-training and training phase ($n = 20$ for WT and $n = 18$ for SRGAP2C mice). (d) Mean water intake per session ($n = 20$ for WT and $n = 18$ for SRGAP2C mice). Bar graphs plotted as s.e.m. (e) Schema showing structure of single trial. Textures rotate and move into position 2 s before opening of the response window (RW). Approximately 1 s before RW opening the texture is within reach of the whiskers, allowing mice to sample the texture while it moves further into position. Upon opening of the RW, correct lick responses lead to a water reward, while incorrect lick responses cause to a time-out. Following RW

closure the texture retracts back out of reach of the whiskers. (f) Example raster plot of an individual mouse showing the distribution of individual licks (red dot for right licks, blue dot for left licks) relative to opening of the response window before (naïve) and after (expert) learning of the task. Correct licks are either right licks (red) for the R2000 texture, or left licks (blue) for the R200 texture. (g) Lick frequency plot for naïve and expert mice. Lick frequency was normalized for each individual mouse to the mean lick frequency before the sampling window. Shaded area around curves indicates s.e.m. (h) Average timing of licking onset in expert mice relative to opening of the response window ($P = 4.91 \times 10^{-2}$; $n = 10$ for WT and $n = 15$ for SRGAP2C mice). Bar graph plotted as mean \pm s.e.m. $*P < 0.05$, two-sided Mann-Whitney test. (i) Fraction of licks from expert mice that are correct relative to opening of the response window. Shaded area around curves indicates s.e.m., two-sided Mann-Whitney test.

Reporting Summary

Nature Research wishes to improve the reproducibility of the work that we publish. This form provides structure for consistency and transparency in reporting. For further information on Nature Research policies, see our [Editorial Policies](#) and the [Editorial Policy Checklist](#).

Statistics

For all statistical analyses, confirm that the following items are present in the figure legend, table legend, main text, or Methods section.

n/a Confirmed

- The exact sample size (n) for each experimental group/condition, given as a discrete number and unit of measurement
- A statement on whether measurements were taken from distinct samples or whether the same sample was measured repeatedly
- The statistical test(s) used AND whether they are one- or two-sided
Only common tests should be described solely by name; describe more complex techniques in the Methods section.
- A description of all covariates tested
- A description of any assumptions or corrections, such as tests of normality and adjustment for multiple comparisons
- A full description of the statistical parameters including central tendency (e.g. means) or other basic estimates (e.g. regression coefficient) AND variation (e.g. standard deviation) or associated estimates of uncertainty (e.g. confidence intervals)
- For null hypothesis testing, the test statistic (e.g. F , t , r) with confidence intervals, effect sizes, degrees of freedom and P value noted
Give P values as exact values whenever suitable.
- For Bayesian analysis, information on the choice of priors and Markov chain Monte Carlo settings
- For hierarchical and complex designs, identification of the appropriate level for tests and full reporting of outcomes
- Estimates of effect sizes (e.g. Cohen's d , Pearson's r), indicating how they were calculated

Our web collection on [statistics for biologists](#) contains articles on many of the points above.

Software and code

Policy information about [availability of computer code](#)

Data collection	NIS-Elements 4.30.02 build 1053 and 5.11.01 build 1367 (Nikon), ThorImage LS 4.0.2019.8191 (Thorlabs), Thorsync 4.0.2019.8191 (Thorlabs), and custom written Python scripts (available upon request).
Data analysis	Prism v6, v8 and v9 (Graphpad), Fiji-ImageJ 1.53c (NIH) with Stackreg version March 2, 2005 and Cell Counter 2.2.2 plugins, Adobe Photoshop CC 2018, NIS-Elements 5.11.01 build 1367 (Nikon), 3DS MAX 2018 with built-in MAXScript (Autodesk), MLspike version April 9, 2020, and custom written scripts in MATLAB R2018a-R2020a (Mathworks) and Python 3.8.5 (available upon request). Python libraries used are matplotlib 3.3.2, numpy 1.19.2, scipy 1.5.2, and sklearn 0.23.2.

For manuscripts utilizing custom algorithms or software that are central to the research but not yet described in published literature, software must be made available to editors and reviewers. We strongly encourage code deposition in a community repository (e.g. GitHub). See the Nature Research [guidelines for submitting code & software](#) for further information.

Data

Policy information about [availability of data](#)

All manuscripts must include a [data availability statement](#). This statement should provide the following information, where applicable:

- Accession codes, unique identifiers, or web links for publicly available datasets
- A list of figures that have associated raw data
- A description of any restrictions on data availability

The datasets generated and/or analyzed during the current study are available from the corresponding author on reasonable request.

Field-specific reporting

Please select the one below that is the best fit for your research. If you are not sure, read the appropriate sections before making your selection.

Life sciences Behavioural & social sciences Ecological, evolutionary & environmental sciences

For a reference copy of the document with all sections, see [nature.com/documents/nr-reporting-summary-flat.pdf](https://www.nature.com/documents/nr-reporting-summary-flat.pdf)

Life sciences study design

All studies must disclose on these points even when the disclosure is negative.

Sample size	No statistical methods were used to predetermine sample sizes. Sample sizes were estimated based on previous experience and are similar to those reported in previous publications (e.g. Charrier and Joshi et al., Cell 2012; Reardon and Murray et al., Neuron 2016; Chen et al., Nature Neuroscience 2015).
Data exclusions	For rabies tracing experiments, animals were excluded using pre-established criteria (all starter neurons need to be located within barrel field of the primary somatosensory cortex). For behavioral experiments, pre-established exclusion criteria were used to exclude mice that did not display performance reduction to <60% correct upon trimming of the whiskers facing the texture meaning that the mouse learn the task in a whisker-independent way. One mouse was excluded using this criterion.
Replication	All experiments were performed with mice from multiple independent litters (at least three) and results were obtained from two or more cohorts, with each cohort showing similar phenotypes.
Randomization	Mice were assigned to their experimental group based on genotype.
Blinding	Experimenters were blinded during data collection and analysis, except for Extended Data Fig. 1f, for which experiments were only performed on heterozygous SRGAP2C mice and therefore blinding for genotype was not possible.

Reporting for specific materials, systems and methods

We require information from authors about some types of materials, experimental systems and methods used in many studies. Here, indicate whether each material, system or method listed is relevant to your study. If you are not sure if a list item applies to your research, read the appropriate section before selecting a response.

Materials & experimental systems

n/a	Involved in the study
<input type="checkbox"/>	<input checked="" type="checkbox"/> Antibodies
<input checked="" type="checkbox"/>	<input type="checkbox"/> Eukaryotic cell lines
<input checked="" type="checkbox"/>	<input type="checkbox"/> Palaeontology and archaeology
<input type="checkbox"/>	<input checked="" type="checkbox"/> Animals and other organisms
<input checked="" type="checkbox"/>	<input type="checkbox"/> Human research participants
<input checked="" type="checkbox"/>	<input type="checkbox"/> Clinical data
<input checked="" type="checkbox"/>	<input type="checkbox"/> Dual use research of concern

Methods

n/a	Involved in the study
<input checked="" type="checkbox"/>	<input type="checkbox"/> ChIP-seq
<input checked="" type="checkbox"/>	<input type="checkbox"/> Flow cytometry
<input checked="" type="checkbox"/>	<input type="checkbox"/> MRI-based neuroimaging

Antibodies

Antibodies used	mouse anti-HA (Anti-HA.11 901513, Biolegend) mouse anti-actin (MAB1501, Millipore) rat anti-somatostatin (MAB354, Millipore) guinea pig anti-parvalbumin (195004, Synaptic Systems) rabbit anti-DsRed (632496, Takara Bio) Secondary antibodies were acquired from Li-Cor (IRDye conjugated) and ThermoFisher Scientific (Alexa conjugated).
Validation	Antibodies have been extensively tested and validated using different cell lines and techniques by corresponding companies. This includes quality control testing of each lot of antibodies by Western blotting. A complete description of antibody validation can be found on each manufacturer's website, including a certificate of quality or analysis, SDS information and extensive list of citations.

Animals and other organisms

Policy information about [studies involving animals](#); [ARRIVE guidelines](#) recommended for reporting animal research

Laboratory animals	Mice of either sex were used in experiments and all mice used in this study were adults (>P65). Transgenic mice included in this study are: Thy1-GCaMP6f-GP5.17Dkim/J obtained from the Jackson Laboratory (JAX 025393). NexCre (NeuroD6tm1(cre)Kan), kindly provided by Dr Klaus-Armin Nave (Max Planck Institute for Experimental Medicine, Göttingen, Germany). Conditional SRGAP2C
--------------------	--

expressing mice were generated using homologous recombination in C57BL/6J mouse ES cells (see Extended Data Fig. 1 and Methods for details) in collaboration with genOway (France). For in utero electroporation experiments, mice were crossed once with the outbred strain 129S2/SvPasCrl mice (obtained from Charles River) to produce F1 hybrids females used to generate timed-pregnant females by crossing with Rosa26SRGAP2C(F/+) heterozygous males (on pure C57BL/6J). This strategy is used because pure C57BL/6J females often cannibalize their offspring at birth following in utero electroporation experiments but not these F1 (C57BL/6J; 129S2/SvPasCrl) females.

Wild animals

No wild animals were used in this study.

Field-collected samples

No field-collected samples were used in this study.

Ethics oversight

All experimental procedures were approved by the Institutional Animal Care and Use Committee (IACUC) of Columbia University, New York.

Note that full information on the approval of the study protocol must also be provided in the manuscript.